Diao, F., Wang, R., Wang, Y., Xiong, X., Walter, T. R. (2018): Fault behavior and lower crustal rheology inferred from the first seven years of postseismic GPS data after the 2008 Wenchuan earthquake. - *Earth and Planetary Science Letters*, *495*, pp. 202—212.

DOI: http://doi.org/10.1016/j.epsl.2018.05.020

Fault behaviour and lower crustal rheology inferred from the first seven years of postseismic GPS data after the 2008 Wenchuan earthquake

Faqi Diao[a], Rongjiang Wang[b*], Yuebing Wang[c], Xiong Xiong[a] and Thomas R. Walter[b]

a. Institute of Geophysics and Geomatics, China University of Geosciences, Wuhan 430074, China

b. GFZ German Research Centre for Geosciences, Telegrafenberg, D-14473 Potsdam, Germany

c. National Earthquake Infrastructure Service, Beijing 100045, China

[*]Corresponding author: Rongjiang Wang (wang@gfz-potsdam.de)

Abstract

Long-term and wide-area geodetic observations may allow identifying distinct postseismic deformation processes following large earthquakes, and thus can reveal fault behaviour and permit quantifying complexities in lithospheric rheology. In this paper, the first 7 years of GPS (Global Positioning System) displacement data following the 2008 Mw7.9 Wenchuan earthquake are used to study the relevant mechanisms of postseismic deformation. Two simple models that consider either afterslip or viscoelastic relaxation as the unitary mechanism of the postseismic deformation are tested at first. After analysing the limitations and complementarity of these two separated models, a combined model incorporating the two main mechanisms is presented. In contrast to previous studies, which mostly assume that afterslip and viscoelastic relaxation are independent, our combined model includes the secondary viscoelastic relaxation effect induced by transient afterslip. Modelling results suggest that the middle- to far-field postseismic deformation is mainly induced by viscoelastic relaxation of the coseismic stress change in the lower crust, whereas the near-field displacement is dominantly caused by stress-driven aseismic afterslip. The seismic moment released by the transient afterslip corresponds to an Mw7.4 earthquake, or 25% of that released by the Mw7.9 main shock. With a characteristic decay time of 1.2 years, most afterslip (~ 80%) is released in the first 2 years. Negligible aseismic afterslip is observed in the seismic gap between the Wenchuan and Lushan earthquakes, indicating the locked state of the fault within this segment. The effective lower crustal viscosity of the eastern Tibetan Plateau is estimated to be 2.0×10^{18} Pa·s, at least two orders of magnitude smaller than that of the adjacent Sichuan Basin. This finding is consistent with previous observations of low seismic velocity and high electrical conductivity in this region, all of which support the assumption that the crustal thickening in the eastern Tibetan Plateau is dominantly caused by ductile lower crustal flow, with important implications for understanding both long- and short-term crustal deformation processes.

Keywords: Wenchuan earthquake, afterslip, viscoelastic relaxation, postseismic deformation, seismic hazard

1. Introduction

Postseismic deformation following large earthquakes has been routinely observed and explained as the response of the lithosphere to coseismic stress redistribution (Bürgmann and Dresen, 2008). The main mechanisms proposed for postseismic deformation include viscoelastic relaxation of coseismically induced stress changes in the ductile lower crust and upper mantle (e.g., Bürgmann and Dresen, 2008; Wang et al. et al., 2012; Freed et al., 2017) and aseismic fault afterslip within or near the coseismic rupture area (e.g., Hsu et al., 2006; Freed, 2007). In addition, the poroelastic rebound effect can also cause observable postseismic deformation, but this mainly occurs in the near-field area with a relatively lower magnitude (Jónsson et al., 2003), which is often ignored due to a lack of observations affected by it. In most cases, aseismic afterslip and viscoelastic relaxation are widely used to interpret postseismic observations. However, due to a similar deformation pattern that is induced by these two mechanisms, it remains challenging to distinguish their relative contributions, especially if the observations have an insufficient temporal and spatial coverage (Bürgmann and Dresen, 2008).

Aseismic afterslip releases stress in weak regions on faults adjacent to coseismic slip asperities (Hsu et al., 2007), potentially reflecting the stress state of the faults. In many previous studies, static or time-dependent afterslip is usually directly derived from surface postseismic displacements via a linear inversion. This approach is convenient and most effective for explaining the observations, but it is not physically based and requires a large number of free parameters. In addition, by ignoring the contribution of viscoelastic relaxation, the obtained afterslip is often overestimated in terms of magnitude and depth (Diao et al., 2014). From recent decades of studies on postseismic deformation, afterslip has been regarded as the dominant mechanism governing the near-field in the initial stage following the earthquake. However, a study on the 2011 Mw9.0 Tohoku earthquake indicates that this paradigm is no longer valid because viscoelastic relaxation can contribute as much as afterslip to postseismic displacements in the first 3.5 years (Freed et al., 2017), suggesting that relative contributions of afterslip and viscoelastic relaxation on postseismic deformation depend on the fault behaviour and regional rheology.

Rheologically weak regions within the lower crust and upper mantle cannot sustain the coseismic stress change and release it in the form of viscoelastic relaxation, which can result in significant crustal deformation (Bürgmann and Dresen, 2008). With measurements of postseismic deformation, the viscosity in regions beneath the coseismic slip area can be explored, which can provide an important *a-priori* information for dynamic studies. Given the nonlinear relation to postseismic displacements, the optimal viscosity value that best fits the data is generally solved using a grid search approach among various forward simulations (Diao et al., 2014; Freed et al., 2017; Huang et al., 2014). Viscoelastic relaxation can generally predict the long-term deformation in the middle- to far-field, but this underestimates observations in the near-field, which implies that other mechanisms might be involved. Considering the limitations of separated afterslip and viscoelastic relaxation models, there has been a consensus that a combined model incorporating these two main mechanisms is more realistic.

On 12 May 2008, the devastating Mw7.9 Wenchuan earthquake occurred on the eastern margin of the Tibetan Plateau adjacent to the Sichuan Basin (Fig. 1), which is a region of high topographic gradient with relatively low strain accumulation rates (Zhang, 2010). Geologic field data, geodetic and seismic monitoring observations have offered valuable constraints on the coseismic slip distribution of the earthquake (e.g., Xu et al., 2009; Shen et al., 2009; Wang et al., 2011). As shown in most slip models, this earthquake first ruptured the southwestern segment with an oblique thrusting slip. Then, the rupture propagated towards the northeast with an increased right-lateral slip component, resulting in a total rupture length of ~ 300 km (Fig. 1). The stress state of the medium surrounding the coseismic rupture was severely changed by the 2008 event and significant postseismic deformation occurred after the earthquake (Shao et al., 2011; Shen et al., 2011; Huang et al., 2014; Xu et al., 2014; Jiang et al., 2017). Observations related to this postseismic deformation are not only unique for understanding the postseismic mechanisms of this earthquake, but also valuable for probing the regional rheology and fault behaviour in the eastern region of the Tibetan Plateau.

The postseismic deformation of the Wenchuan earthquake has been analysed in several previous studies (Huang et al., 2014; Jiang et al., 2017; Shao et al., 2011; Shen et al., 2011; Xu et al., 2014). As summarized in Table 1, all studies except that by Xu et al. (2014) used combined models that incorporate afterslip and viscoelastic relaxation to explain the postseismic displacements. However, the parameters of these combined models, i.e., the lower crustal viscosity and the afterslip distribution, were not determined simultaneously but successively. In these previous studies, a viscoelastic relaxation model is optimized first to fit the accumulated postseismic displacement data without considering the contribution from the afterslip. In the second step, the residual data obtained by subtracting the viscoelastic relaxation effect are inverted for a static afterslip distribution. The time dependence of the afterslip and the secondary effect of viscoelastic relaxation induced by the afterslip are generally neglected. Moreover, previous studies may suffer from the limited spatial and temporal coverage of the observations and the simplified earth models (Table 1).

Here, we present a set of well-distributed postseismic GPS data, which covers the first 7 years following the Wenchuan earthquake. We initially carry out a separate set of 3D viscoelastic relaxation simulations and kinematic afterslip inversions to identify how and to what extent the observations can be explained by each of the two main mechanisms. Then, we demonstrate a combined model incorporating viscoelastic relaxation (due to both coseismic slip and afterslip) and stress-driven afterslip, and we estimate their relative contributions to the observed postseismic deformation. Finally, we discuss the lower crustal viscosity of the Tibetan Plateau and seismic hazards in the southwestern end of the Wenchuan rupture based on the results of this study.

2. GPS Data Processing

Campaign GPS data, which are used to evaluate the postseismic deformation of the Wenchuan earthquake, were collected from 1999 to 2015 by the Crustal Movement

Observation Network of China (CMONOC). Pre-earthquake observations are required to obtain the background tectonic deformation rate, which should be removed to isolate the postseismic transient signals. Therefore, only GPS stations with at least four pre-earthquake surveys that cover a period of ~ 10 years (Fig. S1) were selected for use in this study.

We processed the GPS data following the approach presented in Gan et al. (2007). The daily raw GPS data were first processed to obtain loosely constrained daily coordinates and satellite orbits using the GAMIT software (Herring et al., 2010a). Then, the obtained, loosely constrained daily solutions were combined with loosely constrained global solutions of 80 IGS tracking stations (released by the Scripps Orbital and Position Analysis Center, http://sopac.ucsd.edu/) using the GLOBK software (Herring et al., 2010b), which fix the solutions to the ITRF08 reference frame (Gan et al., 2007).

After the position time series have been achieved, a station-dependent exponential function is employed to describe the time-dependent behaviour of the obtained postseismic displacement time series (Freed et al., 2017),

$$U(t) = U_0 + V_0 \cdot (t - t_{eq}) + \left\{ D_e + D_v \cdot \left[1 - e^{-\frac{(t-t_{eq})}{\tau}} \right] \right\} H(t - t_{eq}) \qquad (1)$$

where t_{eq} (hereafter $t_{eq} = 0$) is the earthquake occurrence time, U_0 is the pre-event station position, V_0 is the regional secular velocity of GPS stations, D_e is the coseismic elastic displacement, D_v is the total postseismic viscoelastic displacement, τ is the characteristic relaxation time, and $H(t)$ is the Heaviside function. The parameters U_0, V_0, D_e, D_v and τ are station dependent and obtained with a non-linear regression of the observed GPS time series. For all selected stations, the secular velocity can be stably estimated from the pre-earthquake observations that were generally surveyed 3-4 times since 1999. Note that a few stations are affected by the coseismic displacements caused by the 2013 Lushan (Mw6.6) and 2014 Kangding (Mw6.2) earthquakes, which have been corrected theoretically based on the slip models inferred from geodetic data (Jiang el al., 2014; Jiang el al., 2015). It should be mentioned that only annual campaign-mode GPS observations are available for this study, and it is known that the effect caused by seasonal hydrological variation is hard to estimate directly from such campaign data. Therefore, we model this effect based on the approach of Chanard et al. (2014) and remove it from the GPS time series, although the resulted correction to the horizontal components (< 2 mm) is rather small.

Because the first postseismic GPS observations in the CMONOC dataset were obtained ~ 1 year after the event (~ 2009.5), the unknown parameters in Eq. (1) are only loosely constrained, especially the characteristic decay time (τ). As shown in Fig. S2 in the supplementary material, a range of curves with different relaxation times can fit the postseismic displacements equally well. The quasi coseismic offsets, which consist of the coseismic offset and the postseismic deformation in the initial few weeks, are important for estimating the unknown parameters in Eq. (1) (Fig. S2). For this reason, the quasi coseismic displacement offsets shown in Wang et al. (2011) are included in our displacement time series, too. All GPS time series in comparison with their regression curves (after removing the pre-event position and the secular trend) are shown in the supplementary material (Fig. S1).

The accumulative postseismic displacements for the first 7 years after the Wenchuan earthquake are shown in Fig. 1b and Table S1, which are derived from the observed time series using the exponential fitting approach, and equal to $D_v \cdot \left[1 - e^{-\frac{7}{\tau}}\right]$ (Fig. S1). The signals are more significant on the hanging wall than on the footwall and show the south-eastward thrusting pattern of the Tibetan Plateau relative to the stable Sichuan Basin. Generally, the postseismic displacement field shows a gentle gradient across the Longmenshan fault (LMSF, Fig. 1b), indicating the likelihood of a fully locked shallow fault after the coseismic rupture.

In comparison, the vertical component of the postseismic data shows a significantly larger uncertainty and a lower signal-to-noise ratio than the two horizontal components (Fig. S1). In addition, the vertical component can be severely influenced by local nontectonic effects (e.g. surface water loading variation and atmospheric pressure), which are hard to remove from the observations in campaign-mode (Fu and Freymueller, 2012). For these reasons, we do not include the vertical displacements to constrain our postseismic model in this study.

3. Modelling Results

Viscoelastic relaxation of the coseismically induced stress change in the lower crust and upper mantle and the aseismic fault slip on the coseismic rupture plane (afterslip) are the two major mechanisms which are widely proposed to explain the postseismic deformation observed after large earthquakes (e.g., Freed et al., 2006; Freed, 2007; Hsu et al., 2006; Ryder et al., 2014). In this section, we investigate how and to what extent the observed postseismic deformation can be explained by these two mechanisms, both separately and jointly.

3.1. Pure Viscoelastic Relaxation Model

The finite element modelling (FEM) software Pylith (Aagaard et al., 2013) is used to simulate the viscoelastic relaxation effect, which is based on a lateral heterogeneous earth structure. The FEM extends for approximately 3000 km and 600 km in the horizontal and depth directions, respectively, to sufficiently minimize the artefacts induced by using the fixed condition at the bottom and side boundaries (Fig. 2a). Based on seismic tomography results (Li et al., 2011), layered structures are defined for either side of the fault (Fig. 2b), which consists of an elastic upper crust and two underlying viscoelastic layers representing the lower crust and upper mantle, and for both, a Maxwell rheology is used (e.g., Freed et al., 2017).

The thickness of the elastic upper crust is set to 35 km for the eastern Tibetan Plateau and 25 km for the Sichuan Basin based on the inferred seismic structure (Li et al., 2011).

A coseismic slip model is imposed as the driving source of the pure viscoelastic relaxation model (PVR). Considering the self-consistency in the methodology and parameter setting used for modelling the co and postseismic deformation, which can avoid potential error propagation (Freed et al., 2017), we re-estimate the coseismic slip distribution by inverting the coseismic GPS data (Wang et al., 2011).

A constrained least squares method (Wang et al., 2013) was employed to infer the coseismic slip model, in which an *a-priori* smoothing constraint was employed to make the result stable. We applied the steepest descent method to search for the optimal solution and defined the cost function as

$$F(s) = \|Gs - y\|^2 + \beta^2\|\mathrm{H}s\|^2 \qquad (2)$$

where s is the slip vector of each sub-fault, G is the Green's function matrix calculated based on an averaged layered earth structure (Li et al., 2011), y is the coseismic GPS displacements; H denotes the finite difference approximation of the Laplacian operator, and β is called the smoothing factor, which controls the trade-off between model roughness and data misfit (Fig. S3). The fault geometry used for the coseismic slip model is slightly modified from that of Wang et al. (2011), which consists of a shallow ramp fault (with a large dip of ~ 55^o) connected by a deep décollement with a small dip angle (7^o). To avoid the unrealistic sudden change of fault dip angle, we defined a listric ramp at depth, which makes the geometry smoother compared to that of Wang et al. (2011) and closer to the geologically inferred listric fault geometry (Zhang et al., 2010).

As will be shown in Section 3.3, the obtained coseismic slip is in general agreement with previous slip models (Shen et al., 2009; Wang et al., 2011). After imposing the coseismic slip model in the FEM, viscosities of the lower crust and upper mantle become the key parameters that influence the model results. Further investigations in this section show that the postseismic surface deformation in the first 7 years is less sensitive to the assumed upper mantle viscosity (Fig. S4). Therefore, we fix the upper mantle viscosities used in the FEM at 1.0×10^{19} Pa·s for the Tibetan Plateau and 1.0×10^{20} Pa·s for the Sichuan Basin following Huang et al. (2014), but the lower crustal viscosities (LCVs) will be optimized to best fit the data.

A grid search approach is used to optimize the lower crustal viscosities of the eastern Tibetan Plateau (η_T) and Sichuan Basin (η_S) in the PVR model. By fitting the observed displacement time series, the misfit function to be minimized is defined by

$$F(\eta_T, \eta_s) = \sum_{i=1}^{M} \sum_{j=1}^{N_i} \sigma_{ij}^{-2} \left[U_{ij} - D_{ij}(\eta_T, \eta_S)\right]^2, \tag{3}$$

where i and j represent the indices of the GPS stations and the station-dependent time samples of the observed time series, respectively, σ is the standard observation error, U and D are the observed and predicted data, respectively. The best-fit viscosities that minimize $F(\eta_T, \eta_s)$ are found to be $\eta_T = 1.0 \times 10^{18}$ Pa·s and $\eta_S \geq 10^{20}$ Pa·s (Fig. 3a). The optimal PVR model can generally explain the middle- to far-field observations (Fig. 3b), but it significantly underestimates the near-field observations.

3.2. Pure Afterslip Model

For testing the pure afterslip (PAS) mechanism, we investigate two different extensions of the fault plane in depth (Fig. 4). In the first model (PAS-1), the fault geometry is constructed by extending the coseismic rupture described in section 3.1. A sub-horizontal décollement fault (with a dip angle of 7° and a width of 90 km) is added at the lower edge of the shallow listric fault to include possible deep slip (Wang et al., 2011). An initial test shows that far-field displacements will be significantly underestimated using this 90-km wide décollement (Fig. S5). We therefore extend the width of the décollement to 300 km for modelling the far-field observation. In the second model (PAS-2), the shallow listric fault is extended to the bottom of the crust (~ 65 km) with a variable dip angle, which decreases with depth from ~ 55° to 5°. From a mechanical point of view, afterslip should appear around or between the coseismic slip asperities rather than in the ductile lower crust. With these two typical but speculative extensions of the fault, we may be able to see whether significant, deep afterslip, though physically unreasonable, are required here to explain the observations.

Compared with model PAS-1, model PAS-2 permits afterslip at larger depths within a narrower zone. For both PAS models, the finite fault is divided into sub-faults with a uniform size of 10 km × 10 km. The afterslip distributions are estimated by inverting the 7-year cumulative postseismic GPS displacement data with the same inversion method (Wang et al., 2013) as used for the coseismic slip inversion in Section 3.1. Green's functions needed for the inversion are calculated based on an average layered earth structure (Li et al., 2011). The elastic inhomogeneity across the fault is neglected here because its influence on the elastic deformation is insignificant (Diao et al., 2014).

The obtained afterslip models and their data fitting are shown in Fig. 4 and Fig. S6. A common and notable feature of both models is the widely distributed afterslip on deep patches of the fault extensions. The postseismic displacements are better fitted by PAS-1 than by PAS-2 (Fig. 4). However, if the width of the horizontal décollement in model PAS-1 is not large enough, the far-field displacements on the hanging wall will be significantly underestimated (Fig. S5). In addition, it should be noted that the apparent afterslip distributions in both models are beyond the depth of the aftershock seismicity (Fig. 4d).

3.3. Combined Model Incorporating Viscoelastic Relaxation and Stress-Driven Afterslip

As mentioned in the Introduction, it has been recognized that viscoelastic relaxation and afterslip could jointly govern the postseismic process (Diao et al., 2014; Huang et al., 2014; Freed et al., 2017). Our results shown in Sections 3.1 and 3.2 also suggest that separated mechanisms either fail to explain the observations or lead to physically unreasonable results. Therefore, a combined model that incorporates afterslip and viscoelastic relaxations is necessary in the present case. Contrary to previous studies that generally assume that the afterslip and viscoelastic relaxation are independent, we consider the viscoelastic relaxation induced by time-dependent afterslip and build the combined model in a more reasonable and realistic way:

(1) As mentioned in Section 3.2, like the aftershocks, afterslip should appear in areas surrounding the large coseismic slip where the Coulomb failure stress (CFS) is dramatically raised by coseismic stress adjustment (e.g., Hsu et al., 2006). Therefore, it can be assumed that afterslip is potentially induced by the coseismic stress change. Following this assumption, we fix the spatial pattern of the afterslip to be the same as the positive coseismic CFS change. The latter is calculated based on the coseismic slip model obtained in Section 3.1 (Figs. 5a and S7). A uniform frictional coefficient of 0.5 is assumed, but a range of values for this parameter (0.2~0.8) were tested to confirm that the pattern of CFS change remains stable. Areas of high coseismic slip (Fig. 5a) show a clear drop in CFS, whereas the adjacent patches around them are stress-enhanced (Fig. 5b).

(2) Following the exponential model used in Eq. (1), we assume that the rate of afterslip decays exponentially and uniformly with time,

$$\dot{s}(\boldsymbol{r},t) = \dot{s_0}(\boldsymbol{r}) \cdot e^{-\frac{t}{\tau}}, \qquad (t > 0), \tag{4}$$

where $\boldsymbol{r}$ is the spatial location of the afterslip, $\dot{s_0}(\boldsymbol{r})$ is the initial afterslip rate that is assumed to be proportional to the positive coseismic CFS change, τ is the uniform characteristic decay time. After fixing the spatial and temporal pattern of the afterslip, the magnitude of afterslip is related to the positive coseismic CFS change (ΔS) with a scaling factor (α),

$$\int_0^T \dot{s}(r,t')dt' = \alpha \cdot max[\Delta S(\boldsymbol{r}), 0], \tag{5}$$

where T is the observation period (here 7 years). Thus, the space and time dependent afterslip is controlled by only two free parameters, i.e., the scaling factor α and the decay time τ.

(3) The transient postseismic displacements predicted by the combined model that incorporates viscoelastic relaxation and afterslip can be expressed in the form

$$D(\boldsymbol{r},t) = D_{cv}(\boldsymbol{r},t) + \alpha\left[D_{ae}(\boldsymbol{r})\tau\left(1-e^{-\frac{t}{\tau}}\right)+\int_0^t D_{av}(\boldsymbol{r},t')e^{-\frac{(t-t')}{\tau}}dt'\right], \quad (6)$$

where $D_{cv}(\boldsymbol{r},t)$ represents the postseismic viscoelastic displacement due to the viscoelastic relaxation induced by the coseismic slip, $D_{ae}(\boldsymbol{r})$ and $D_{av}(\boldsymbol{r},t)$ are the afterslip-induced elastic and viscoelastic displacements, respectively. All the three variables D_{cv}, D_{ae} and D_{av} are calculated using the same FEM and fault geometry described in Section 3.1.

(4) As known from Section 3.1, the lower crustal viscosity of Sichuan Basin can only be constrained with a lower bound at about 1.0×10^{20} Pa·s (Fig. 3a). Therefore, we fix this parameter to further reduce the degrees of freedom of the combined model. Finally, the combined model is controlled by three parameters, i.e., the lower crustal viscosity of the Tibetan Plateau (η_T), the scaling factor (α) and the decay time (τ) for afterslip, which need to be optimized by minimizing the misfit function of the whole displacement time series, as defined by Eq. (3),

$$F(\eta_T,\alpha,\tau) = \sum_{i=1}^{M}\sum_{j=1}^{N_i}\sigma_{ij}^{-2}\left[U_{ij}-D_{ij}(\eta_T,\alpha,\tau)\right]^2. \quad (7)$$

It should be noted that only the viscosity η_T and the decay time τ are nonlinearly related to the data. For any given combination of η_T and τ, the scaling factor α can be determined uniquely by the linear approach. Therefore, the present 3D nonlinear fitting problem is actually solved with a grid search in a 2D parameter space.

The best-fit lower crustal viscosity for the Tibetan Plateau is found to be $\eta_T = 2.0 \times 10^{18}$ Pa·s, which is twice as large as that of the PVR model (Figs. 3a and 6a). The best-fit decay time of the afterslip is given by $\tau \sim 1.2$ years, which implies that more than 80% of the afterslip was released already within the first 2 years after the event (Fig. S8). The consequent best-fit scaling factor between the magnitude of afterslip and the positive coseismic CFS change is $\alpha = 0.35$ m/MPa, which results in the afterslip distribution shown in Fig. 5c and Fig. S7. The viscosity η_T and the scaling factor α are better resolved than the decay time τ (Figs. 6a-c). The reasons are the insufficient time sampling rate and limited data length.

The seismic moment released by the afterslip is 1.6×10^{20} Nm, ~ 25% of that of the main shock and corresponding to an Mw7.4 earthquake. We found that most of the afterslip is distributed at the down-dip extension of the coseismic rupture, whereas the local afterslip is observed on shallow patches among the coseismic slip concentrations. The aftershocks with $M \geq 3$ for the same 7-year period (data obtained from China Earthquake Networks Center, http://www.csndmc.ac.cn/newweb/data.htm#, last accessed on 01/08/2017), released only ~ 1.1% of the seismic moment of the main shock, which indicates that the moment release during the postseismic process is essentially aseismic.

The predicted postseismic displacements of the combined model match the data well in terms of total magnitude (Fig. 6d) and temporal evolution (Fig. 7 and Fig. S1). The complementary contributions from the two main mechanisms can be revealed as expected, i.e., the near-field postseismic deformation is mainly caused by the stress-driven afterslip, whereas in the middle- to far-field it appears to be more controlled by the viscoelastic relaxation (Fig. 7). In the time domain, the contribution from the afterslip is mostly accomplished in the initial 2 years, whereas the contribution from the viscoelastic relaxation is sustained and plays a dominant role on the postseismic displacements in the following periods (Fig. 7).

4. Discussion

4.1. Joint Process of Viscoelastic Relaxation and Stress-Driven Afterslip

To explain the far-field postseismic deformation, widespread, deep afterslip beyond the depth of most aftershocks (Fig. 4) appears to be required by the two pure afterslip models. However, the low-velocity anomalies at these depths (e.g., Pei et al., 2014; Wang et al., 2015) imply ductile rock materials, which might not be able to generate brittle dislocations (Pei et al., 2014). Thus, despite both PAS models providing a satisfactory fit to the data, they are physically unreasonable. The apparent widespread deep afterslip only indicates the spatial extension of the driving source. In contrast, the pure viscoelastic model can reasonably explain the data in the middle to far-field, but it fails in the near-field, which suggests that the afterslip cannot be completely ruled out.

The combined model that incorporates viscoelastic relaxation in the lower crust and stress-driven afterslip on the coseismic rupture plane can overcome the limitations of the unitary mechanisms. In the case of the Wenchuan earthquake, stress-driven afterslip is mostly concentrated at depths less than 30 km, which is close to the depth of the aftershock cloud (Fig. 4d). Moreover, we observe that the stress-driven afterslip exhibits a closer spatial correlation with the aftershock seismicity than the free afterslip derived from the residual data of the pure viscoelastic relaxation model (Figs. 5e and 5f), indicating that the combined model works better, even with only three free parameters (η_T, α, τ).

The temporal evolution of the afterslip should be considered to incorporate the secondary viscoelastic relaxation induced by it. In this study, we assume that the rate of afterslip decays exponentially with time. It should be noted that the mathematical form of the afterslip rate is not unique and other functions have been used to describe the temporal history of afterslip. For example, Helmstetter and Shaw (2009) adopted the same Omori law of the aftershock seismicity for the afterslip rate, $\dot{s}(t) \propto 1/(1+t/\tau)^p$, $(p \sim 1)$. To test the stability of our results, we also tested the performance of the Omori law for the afterslip rate in the present case. As a result, we find that the corresponding optimal lower crustal viscosity of the eastern Tibetan Plateau (η_T) and scaling factor (α) remains the same as that inferred from the exponential form. The optimal Omori decay time is found to be ~0.18 year that is in fact comparable with the exponential decay time of 1.2 years (Fig. S8).

In most previous studies, afterslip is normally assumed to be independent from viscoelasticity and therefore only its elastic deformation is considered (Freed et al., 2007). However, afterslip itself should in principle induce viscoelastic relaxation t in addition to that driven by the coseismic slip. To compare the three different effects on the postseismic deformation, i.e., the viscoelastic effect induced by the coseismic slip, the elastic and viscoelastic effects induced by the afterslip, we calculate surface displacements on a profile perpendicular to the earthquake fault using the optimal combined model. As shown in Fig. 7a, the displacement induced by the viscoelastic effect of the afterslip can reach ~2 cm on the hanging wall, ~ 15% of the total postseismic displacements in the first 7 years after the Wenchuan earthquake. Generally, this effect contributes ~ 8-15% of the total deformation in the period, which is comparable with the results from the postseismic study of the 2011 Tohoku earthquake by Freed et al. (2017). Furthermore, it is notable that the afterslip and viscoelastic relaxation should co-evolve, i.e., not only will there be viscoelastic relaxation caused by the afterslip, but also the viscoelastic relaxation would change the stress conditions under which the afterslip occurs. To evaluate the influence of the latter, we calculate the CFS change caused by coseismic viscoelastic relaxation. As shown in the Fig. S9, the stress induced by coseismic viscoelastic relaxation is rather small compared with that induced by sudden coseismic slip (< 7% in the first two years). Therefore, the coseismic CFS change plays a dominant role in governing the spatial pattern of the afterslip, whereas that induced by viscoelastic relaxation within the observation period considered in this study is negligible.

4.2. Lateral Inhomogeneity of the Lower Crustal Viscosity across the LMS

The lower crust beneath the eastern Tibetan Plateau has been characterized by low seismic velocity and high electrical conductivity that may be attributed to high temperatures and elevated fluid content (e.g., Bai et al., 2010; Pei et al., 2014). The large contrast in the lower crustal viscosity across the Longmenshan fault, which is inferred from the postseismic GPS data in this study, suggests a weak, lower crust beneath the eastern Tibetan Plateau in contrast to the stable Sichuan Basin, and it is therefore consistent with previous seismic and magnetotelluric results.

Postseismic geodetic data have also been used for investigating the transient lower crustal viscosity beneath the Tibetan Plateau. The obtained effective lower crustal viscosity generally increases with time during the postseismic deformation process (Fig. 8), which is consistent with the stress-dependent behaviour inferred from laboratory experiments (e.g., Freed et al., 2006). This time and stress-dependent behaviour may provide a clue to reconciling the difference between the effective viscosities inferred from postseismic data over short time scales and that from geodynamic/geological models over longer time scales (Clark and Royden, 2000). In addition, it should be noted that the lower crustal viscosity of the Tibetan Plateau inferred from the combined model is higher than that of the pure viscoelastic relaxation model (Figs. 3a and 6a), which indicates that ignoring the afterslip effect may lead to an underestimation of the lower crustal viscosity.

Lateral variations in the crustal viscosity may exist, as other studies in the northeast Tibetan Plateau suggest (Ryder et al., 2011; Wen et al., 2012). Speculating that such heterogeneities might also occur elsewhere, possibly on different scales, complexity in postseismic deformation can be expected for adjacent active faults. Moreover, lateral variations of viscosity will change the strength of crust, and affect the pattern of fault deformations at different stages of a seismic cycle, which might warrant further studies in the future.

4.3. Seismic Hazard Assessment at the Extensions of the Wenchuan Rupture

The combined model indicates shallow afterslip on the northeastern extension of the coseismic rupture (Figs. 5d and 5e), which agrees with the near-field postseismic InSAR (Interferometric Synthetic Aperture Radar) observations that reveal short wavelength deformation across this fault segment (Huang et al., 2014). The shallow aftershocks also suggest that the shallow part of this segment was active under the loading of deep coseismic slip (Luo et al., 2010). Combined with this evidence, we infer that the stress on the Qingchuan segment might have been released (Fig. 5e), whereas the stress on the more northern segment (> 32.5^{o} N) could be enhanced.

Compared to the north-eastern segments, the southwestern extension of the Wenchuan rupture has attracted more attention because the 2013 Mw6.6 Lushan earthquake left a 50-km-long seismic gap (Fig. 1). The fault behaviour and related seismic hazards of this segment have been subject to debate. Low seismic velocity anomalies in this area that inferred from geophysical observations suggest that this segment might not be strong enough to generate brittle deformation (e.g., Pei et al., 2014; Wang et al., 2015). However, geological studies indicated that historical earthquakes have in fact ruptured this segment (Dong et al., 2017; Wang et al., 2014).

In this study, negligible afterslip is observed on this seismic gap (Fig. 5c and 5e), which indicates that this fault segment may be locked. This result is obviously confirmed by the near-field displacement time series of station QLAI (Fig. S10), which indicates that the eastward motion on the footwall has increased instead of decreased after the Wenchuan earthquake. Moreover, the absence of aftershocks in the region also contradicts the afterslip hypothesis. The Lushan earthquake is generally believed to have been triggered by the

Wenchuan earthquake (Jia et al., 2014) or even regarded as a strong aftershock of the latter (Zhu, 2016). Our observations reveal that the locked fault segment between the two successive major earthquakes either acts as a barrier that resists rupture propagation, or it has not yet accumulated a sufficient slip deficit. The latter seems more reasonable as historical earthquakes have ruptured this segment (Dong et al., 2017; Wang et al., 2014).

Similar seismic gaps between two adjacent successive ruptures have been observed both on continental faults and in subduction zones (e.g., Delouis et al., 2010). These gaps perhaps were caused by separated asperities, which remain locked to accumulate strain for the next rupture even under the boost of adjacent events. Such rupture segmentation along a fault could be due to fault geometry complexities (Hubbard et al., 2016), frictional behaviour (Manighetti et al., 2007) or different fault locking degrees (Moreno et al., 2011).

4.4 Limitations

In this study, we investigate separated and combined postseismic mechanisms based on the GPS displacements in first 7 years following the Wenchuan earthquake. Due to the spatial and temporal complexity of the co-evolved processes, we fix the spatial pattern of afterslip to decrease the degree of freedom in the combined model by assuming that afterslip is potentially controlled by coseismic CFS change. This assumption is made following a general consensus that afterslip is mostly distributed in areas surrounding the coseismic slip asperity, where the coseismic CFS are clearly enhanced. Besides the loading of the coseismic rupture, the CFS is also affected by the pre-seismic stress state of the fault. However, due to the lack of efficient observations, the pre-seismic stress state on the LMSF is not available and remains hard to estimate. Therefore, we assume that the afterslip is governed by the coseismic CFS change and the effect of pre-seismic stress state is negligible. As shown by the results, the combined model can explain the observation well in terms of the total amplitude and the temporal evolution (Fig. 6d and Fig. S1). Moreover, the stress-driven afterslip exhibits a closer spatial correlation with the aftershock seismicity than the free afterslip derived from the residual data of the pure viscoelastic relaxation model (Figs. 5e and 5f), suggesting that this assumption works as a first-order approximation.

In addition, the inferred coseismic CFS change depends on the inverted coseismic slip model, which may vary by using different inversion approaches and model configurations (Shen et al., 2009; Wang et al., 2011 and many others). For example, the choose of the smoothing factor [see Eq. (2)], which controls the spatial roughness of the coseismic slip model, could change the coseismic slip distribution, especially for some local slip asperities (Wang et al., 2011). To investigate how the CFS change will be affected by the coseismic slip model, we choose different smoothing factors to infer coseismic slip model, and calculate the corresponding CFS change. As shown in Fig. S3, the first-order pattern of the CFS change remains stable though the coseismic slip model changes with the smoothing factors varying near the corner of the trade-off curve.

Finally, it should be mentioned that the poroelastic rebound effect of the permeable uppermost crust is ignored in this study. In fact, the magnitude of poroelastic contribution to the postseismic deformation can be estimated based on the simple approach as presented in, e.g., Huang et al. (2014). In this approach, the complete poroelastic rebound effect can be evaluated using the difference of elastic coseismic displacements associated with variable Poisson ratios under undrained and drained conditions. Our test model for the poroelastic effect has the same layering structure as the elastic one used for the coseismic slip inversion, but the uppermost part (up to 4 km) is assumed to be poroelastic. The Poisson ratio of this layer can vary by up to 30% depending on whether it is under drained or undrained conditions. Using the Poisson ratio of 0.25 under undrained conditions (the original seismic reference) and 0.21 under drained conditions, the model results show that the postseismic displacement caused by poroelastic rebound effect is dominated by the vertical component and the maximum of the long-term accumulative value is estimated to be about 1 cm, which is at least by one order of magnitude smaller than the observed accumulative displacements in the first 7 years after the Wenchuan earthquake. We also test different thickness (2-4 km) of the poroelastic layer, but found no substantial change on the results. Therefore, we ignored the poroelastic rebound effect in our models.

5. Conclusions

Using the GPS observations acquired during the first 7 years after the 2008 Wenchuan earthquake, the related mechanisms are investigated, which include lower crustal viscoelastic relaxation, afterslip and a combination of both. In contrast to previous postseismic studies, we built a combined model that incorporates the viscoelastic relaxation induced by both the coseismic slip and stress-driven afterslip. The secondary viscoelastic relaxation induced by afterslip is found to have a significant effect on both near- and far-field postseismic displacements and therefore should be considered for the postseismic analysis of large earthquakes elsewhere. Lower crustal viscoelastic relaxation is found to be responsible for most of the middle- to far-field postseismic deformation, while the near-field displacements are governed mainly by the stress-driven afterslip. The estimated seismic moment released by stress-driven afterslip is up to 25% of that released by the coseismic rupture, which is equivalent to an Mw7.4 earthquake. Negligible afterslip is observed in the seismic gap between the Wenchuan and Lushan ruptures. Combined with the observation of very low aftershock seismicity during the same period, we deduce that this segment is in a locked state. The effective lower crustal viscosity of the eastern Tibetan Plateau is estimated to be 2.0×10^{18} Pa·s, whereas that of the Sichuan Basin should be larger than 1.0×10^{20} Pa·s, suggesting a significant lateral viscosity contrast across the LMS fault.

Acknowledgments

This work was supported by the National Natural Science Foundation of China (Grant Nos. 41674023 and 41731072) and the China Earthquake Science Experiment Program (2017CESE0103). The data were obtained from the Crustal Movement Observation Network of China (CMONOC). Jeffrey Freymueller and an anonymous reviewer provided valuable comments and suggestions to improve the quality and readability of the revised manuscript. We thank Kevin Fleming, Jing Zeng-Liu, and Yanqiang Wu for their valuable comments on the original manuscript. The figures are drawn using the Generic Mapping Tools (GMT) software (Wessel and Smith, 1998).

References

Aagaard, B.T., Knepley, M.G., Williams, C.A., 2013. A domain decomposition approach to implementing fault slip in finite-element models of quasi-static and dynamic crustal deformation. J. Geophys. Res., Solid Earth. 118, 3059-3079, doi:10.1002/jgrb.50217.

Bai, D., Unsworth, M.J., Meju, M.A., Ma, X., Wen, J., Kong, X., Sun, Y., Sun, J., Wang, L., Jiang, C., Zhao, C., Xiao, P., Liu M., 2010. Crustal deformation of the eastern Tibetan plateau revealed by magnetotelluric imaging. Nat. Geosci. 3, 358-362, doi: 10.1038/NGEO830.

Bürgmann, R., Dresen, G., 2008. Rheology of the lower crust and upper mantle: Evidence from rock mechanics, geodesy, and field observations. Ann. Rev. Earth Planet. Sci. 36, 531-567, doi:10.1146/annurev.earth.36.031207.124326.

Chanard, K., Avouac J. P., Ramillien G., Genrich J., 2014. Modeling deformation induced by seasonal variations of continental water in the Himalaya region: Sensitivity to Earth elastic structure. J. Geophys. Res. Solid Earth 119, 5097–5113, doi:10.1002/2013JB010451.

Clark, M.K., Royden, L.H., 2000. Topographic ooze: Building the eastern margin of Tibet by lower crustal flow. Geology 28, 703-706.

Delouis, B., Nocquet J.M., Vallée, M., 2010. Slip distribution of the February 27, 2010 Mw = 8.8 Maule Earthquake, central Chile, from static and high-rate GPS, InSAR, and broadband teleseismic data. Geophys. Res. Lett. 37, L17305, doi: 10.1029/2010GL043899

Diao, F., Xiong, X., Wang, R., Zheng, Y., Walter, T.R., Weng, H., Li, J., 2014. Overlapping postseismic deformation processes: Afterslip and viscoelastic relaxation following the 2011 Mw 9.0 Tohoku (Japan) earthquake. Geophys. J. Int. 196, 218-229, doi:10.1093/gji/ggt376.

Dong, S., Han, Z., An, Y., 2017. Paleoseismological events in the ‘‘seismic gap” between the 2008 Wenchuan and the 2013 Lushan earthquakes and implications for future seismic potential. J. Asian Earth Sci. 135, 1-15, doi: 10.1016/j.jseaes.2016.12.016.

Fang, L.H., Wu, J., Wang, W., Du, W., Su, J., Wang, C., Yang, T., Cai, Y., 2015. Aftershocks observation and analysis of the 2013 Ms 7.0 Lushan earthquakes. Seismol. Res. Lett. 86(4), 1135-1142, doi: 10.1785/0220140186.

Freed, A.M., 2007. Afterslip (and only afterslip) following the 2004 Parkfield, California earthquake. Geophys. Res. Lett., 34(6), L06312, doi: 10.1029/2006GL029155.

Freed, A.M., Bürgmann, R., Calais, E., Freymueller, J., 2006. Stress-dependent power-law flow in the upper mantle following the 2002 Denali, Alaska, earthquake. Earth Planet. Sci. Lett. 252, 481-489, doi: 1016/j.epsl.2006.10.011.

Freed, A.M, Hashima, A., Becker, T.W., Okaya, D.A., Sato, H., Hatanaka, Y., 2017. Resolving depth-dependent subduction zone viscosity and afterslip from postseismic displacements following the 2011 Tohoku-oki, Japan earthquake. Earth Planet. Sci. Lett. 459, 279-290, doi: 10.1016/j.epsl.2016.11.040.

Fu, Y., Freymueller, J.T., 2012. Seasonal and long-term vertical deformation in the Nepal Himalaya constrained by GPS and GRACE measurements. J. Geophys. Res. 117, B03407, doi: 10.1029/2011JB008925.

Gan, W., Zhang, P., Shen, Z.-K., Niu, Z., Wang, M., Wan, Y., Zhou, D., Cheng, J., 2007. Present-day crustal motion within the Tibetan Plateau inferred from GPS measurements. J. Geophys. Res., 112, B08416, doi:10.1029/2005JB004120.

Helmstetter, A., Shaw, B.E., 2009. Afterslip and aftershocks in the rate-and-state friction law. J. Geophys. Res. 114, B01308, doi: 10.1029/2007JB005077.

Herring, T.A, King, R.W., McClusky, S.C., 2010a. GAMIT Reference Manual. GPS Analysis at MIT. Release 10.4. Massachussetts Institute Technology, http://www-gpsg.mit.edu/~simon/gtgk/index.htm.

Herring, T.A, King, R.W., McClusky, S.C., 2010b. GLOBK Reference Manual: Global Kalman filter VLBI and GPS analysis program. Release 10.4. Massachusetts Institute of Technology, http://www-gpsg.mit.edu/∼simon/gtgk/index.htm.

Hsu, Y.J., Simons, M., Avouac, J.P., Galetzka, J., Sieh, K., Chlieh, M., Natawidjaja, D., Prawirodirdjo, L., Bock, Y., 2006. Frictional afterslip following the Mw 8.7, 2005 Nias-Simeulue earthquake, Sumatra. Science 312, 1921-1926, doi: 10.1126/science.1126960.

Huang, M.H., Bürgmann, R., Freed, A., 2014. Probing the lithospheric rheology across the eastern margin of the Tibetan Plateau. Earth Planet. Sci. Lett. 396, 88-96, doi:10.1016/j.epsl.2014.04.003.

Hubbard, J., Almeida, R., Foster, A., Sapkota, S.N., Bürgi, P., Tapponnier, P., 2016. Structural segmentation controlled the 2015 Mw 7.8 Gorkha earthquake rupture in Nepal. Geology 44 (8), 639-642, doi: 10.1130/G38077.1.

Jia, K., Zhou, S., Zhuang, J., Jiang, C., 2014. Possibility of the Independence between the 2013 Lushan Earthquake and the 2008 Wenchuan Earthquake on Longmen Shan Fault, Sichuan, China. Seismol. Res. Lett. 85, 60-67, doi: 10.1785/0220130115.

Jiang, G., Wen, Y., Liu, Y., Xu, X., Fang, L., Chen, G., Gong, M., Xu, C., 2015. Joint analysis of the 2014 Kangding, southwest China, earthquake sequence with seismicity relocation and InSAR inversion. Geophys. Res. Lett. 42, 3273–3281, doi: 10.1002/2015GL063750.

Jiang, Z., Wang, M., Wang, Y., Wu, Y., Che, S., Shen, Z.K., Bürgmann, R., Sun, J., Yang, Y., Hua, L., Li, Q., 2014. GPS constrained coseismic source and slip distribution of the 2013 Mw6.6 Lushan, China, earth-quake and its tectonic implications. Geophys. Res. Lett. 41, 407-413, doi: 10.1002/2013GL058812.

Jiang, Z., Yuan, L., Huang, D., Yang, Z., Chen, W., 2017. Postseismic deformation associated with the 2008 Mw 7.9 Wenchuan earthquake, China: Constraining fault geometry and investigating a detailed spatial distribution of afterslip. J. Geody. 112, 12–21, doi: 10.1016/j.jog.2017.09.001

Jónsson, S., Segall, P., Pedersen, R., Björnsson, G., 2003. Post-earthquake ground movements correlated to poro-pressure transients. Nature 424, 179-183, doi: 10.1038/nature01776.

Li, Z., Xu, Y., Huang, R.Q., Qiu, R., Hao, T.Y., Xu, Y., Liu, J.S., Liu, J. H., 2011. Crustal P-wave velocity structure of the Longmenshan region and its tectonic implications for the 2008 Wenchuan earthquake. Sci. China Earth Sci. 54, 1386-1393, doi: 10.1007/s11430-011-4177-2.

Luo, Y., Ni, S.D., Zheng, X. F., Zheng, Y., Chen, Q. F., Chen, Y., 2010. A shallow aftershock sequence in the north-eastern end of the Wenchuan earthquake aftershock zone. Sci. China Earth Sci. 53(11), 1655-1664, doi: 10.1007/s11430-010-4026-8.

Manighetti, I., Campillo, M., Bouley, S., Cotton, F., 2007. Earthquake scaling, fault segmentation, and structural maturity. Earth Planet. Sci. Lett. 253(3–4), 429–438, doi: 10.1016/j.epsl.2006.11.004.

Moreno, M., Melnick, D., Rosenau, M., Bolte, J., Klotz, J., Echtler, H., Baez, J., Bataille, K. Chen, J., Bevis, M., Hase, H., Oncken, O., 2011. Heterogeneous plate locking in the South-Central Chile subduction zone: building up the next great earthquake. Earth Planet. Sci. Lett. 305 (3–4), 413-424, 10.1016/j.epsl.2011.03.025.

Pei, S., Zhang, H., Su, J., Cui, Z., 2014. Ductile gap between the Wenchuan and Lushan earthquakes revealed from the two-dimensional Pg seismic tomography. Sci. Rep. 4, 6489, doi: 10.1038/srep06489.

Ryder, I., Bürgmann, R., Pollitz, F., 2011. Lower crustal relaxation beneath the Tibetan Plateau and Qaidam Basin following the 2001 Kokoxili earthquake. Geophys. J. Int. 187 (2), 613-630.

Ryder, I., Bürgmann, R., Sun, J., 2010. Tandem afterslip on connected fault planes following the 2008 Nima-Gaize (Tibet) earthquake. J. Geophys. Res. 115, B03404, doi: 10.1029/2009JB006423.

Ryder, I., Parsons, B., Wright, T.J., Funning, G.J., 2007. Post-seismic motion following the 1997 Manyi (Tibet) earthquake: InSAR observations and modelling. Geophys. J. Int. 169, 1009-1027, doi:10.1111/j.1365-246X.2006.03312.x.

Ryder, I., Wang, H., Bie, L., Rietbrock, A., 2014. Geodetic imaging of late postseismic lower crustal flow in Tibet. Earth Planet. Sci. Lett. 404, 136-143, doi:10.1016/j.epsl.2014.07.026.

Shao, Z., Wang, R., Wu, Y., Zhang, L., 2011. Rapid afterslip and short-term viscoelastic relaxation following the 2008 Mw7.9 Wenchuan earthquake. Earthquake Sci. 24, 163-175.

Shen, Z.K., Sun, J., Zhang, P., Wan, Y., Wang, M., Bürgmann, R., Zeng, Y., Gan, W., Liao, H., Wang, Q., 2009. Slip maxima at fault junctions and rupturing of barriers during the 2008 Wenchuan earthquake. Nat. Geosci. 2, 718-724, doi: 10.1038/NGEO636.

Shen, Z.K, Wang, M., Wang, Y., Wan, Y., Zhang, P., Sun, J., Tao, W., Wang, Y., Wang, K., Hao, M., 2011. Postseismic deformation of the 2008 Mw 7.9 Wenchuan earthquake and its tectonic implications. American Geophysical Union, Fall Meeting 2011, San Francisco, CA, Abstract #T31E-07.

Shen, Z.K, Zeng, Y., Wang, M., Wang, Q., Wang, Q.L., Wan, Y., Gan, W., Zhang, Z., 2003. Postseismic deformation modeling of the 2001 Kokoxili earthquake, western China. EGS - AGU - EUG Joint Assembly, Abstracts from the meeting held in Nice, France, 6 - 11 April 2003, abstract #7840.

Wang, H., Chen, L., Ran, Y., Lei, S., Li, X., 2014. Paleoseismic investigation of the seismic gap between the seismogenic structures of the 2008 Wenchuan and 2013 Lushan earthquakes along the Longmen Shan fault zone at the eastern margin of the Tibetan Plateau. Lithos. 7, 14-20, doi: 10.1130/L373.1.

Wang, K., Hu, Y., He, J., 2012. Deformation cycles of subduction earthquakes in a viscoelastic Earth. Nature 484, 327-332, doi: 10.1038/nature11032.

Wang, Q, Qiao, X., Lan, Q., Jeffrey, F., Yang, S., Xu, C., Yang, Y., You, X., Tan, K., Chen, G., 2011. Rupture of deep faults in the 2008 Wenchuan earthquake and uplift of the Longmen Shan. Nat. Geosci. 4, 634-640, doi: 10.1038/NGEO1210.

Wang, R., Diao, F., Hoechner, A., 2013. SDM - A geodetic inversion code incorporating with layered crust structure and curved fault geometry. Geophysical Research Abstracts, 15, EGU2013-2411-1.

Wang, Z., Su, J., Liu, C., Cai, X., 2015. New insights into the generation of the2013 Lushan Earthquake (Ms7.0), China. J. Geophys. Res., Solid Earth 120, 3507-3526, doi: 10.1002/2014JB011692.

Wen, Y., Li, Z., Xu, C., Ryder, I., Bürgmann, R., 2012. Postseismic motion after the 2001 MW 7.8 Kokoxili earthquake in Tibet observed by InSAR time series. J. Geophys. Res. 117, B08405, doi: 10.1029/2011JB009043.

Wessel, P., Smith, W.H.F., 1998. New improved version of Generic Mapping Tools released. Eos. Trans. AGU 79, 579, doi: 10.1029/98EO00426.

Xu, C., Fan, Q.B., Wang, Q., Yang, S.M., Jiang, G.Y., 2014. Potseismic deformation after the 2008 Wenchuan earthquake. Survey Review 46(339):432-436, doi: 10.1179/1752270614Y.0000000128.

Xu, X., Wen, X., Yu, G., Chen, G., Klinger, Y., Hubbard, J., Shaw, J., 2009. Co-seismic reverse- and oblique-slip surface faulting generated by the 2008 Mw 7.9 Wenchuan earthquake, China. Geology 37(6), 515-518, doi: 10.1130/G25462A.1.

Zhang, C., Cao, J., Shi, Y., 2009. Studying the viscosity of lower crust of Qinghai-Tibet Plateau according to post-seismic deformation. Sci. China, Ser. D. 52(3), 411-419, doi: 10.1007/s11430-009-0028-9.

Zhang, P. Z., Wen, X. Z., Shen, Z. K., Chen, J. H., 2010. Oblique high-angle listric-reverse faulting and associated straining processes: the Wenchuan earthquake of 12 May 2008, Sichuan, China. Annu. Rev. Earth Planet. Sci. 38, 353–382.

Zhu, S., 2016, Is the 2013 Lushan earthquake (Mw = 6.6) a strong aftershock of the 2008 Wenchuan, China mainshock (Mw = 7.9)? J. Geodyn. 99, 16-26, doi: 10.1016/j.jog.2016.05.002.

Supplementary Material

for

Fault behaviour and lower crustal rheology inferred from the first seven years of postseismic GPS data after the 2008 Wenchuan earthquake

Faqi Diao[a], Rongjiang Wang[b*], Yuebing Wang[c], Xiong Xiong[a] and Thomas R. Walter[b]

a. Institute of Geophysics and Geomatics, China University of Geosciences, Wuhan 430074, China

b. GFZ German Research Centre for Geosciences, Telegrafenberg, D-14473 Potsdam

c. National Earthquake Infrastructure Service, Beijing, 100045, China

[*]Corresponding author: Rongjiang Wang (wang@gfz-potsdam.de)

Contents of this file

Introduction

Figures S1-10 show the 7-years GPS time series and additional model results, and Table S1 lists the cumulative postseismic displacements measured at all selected stations.

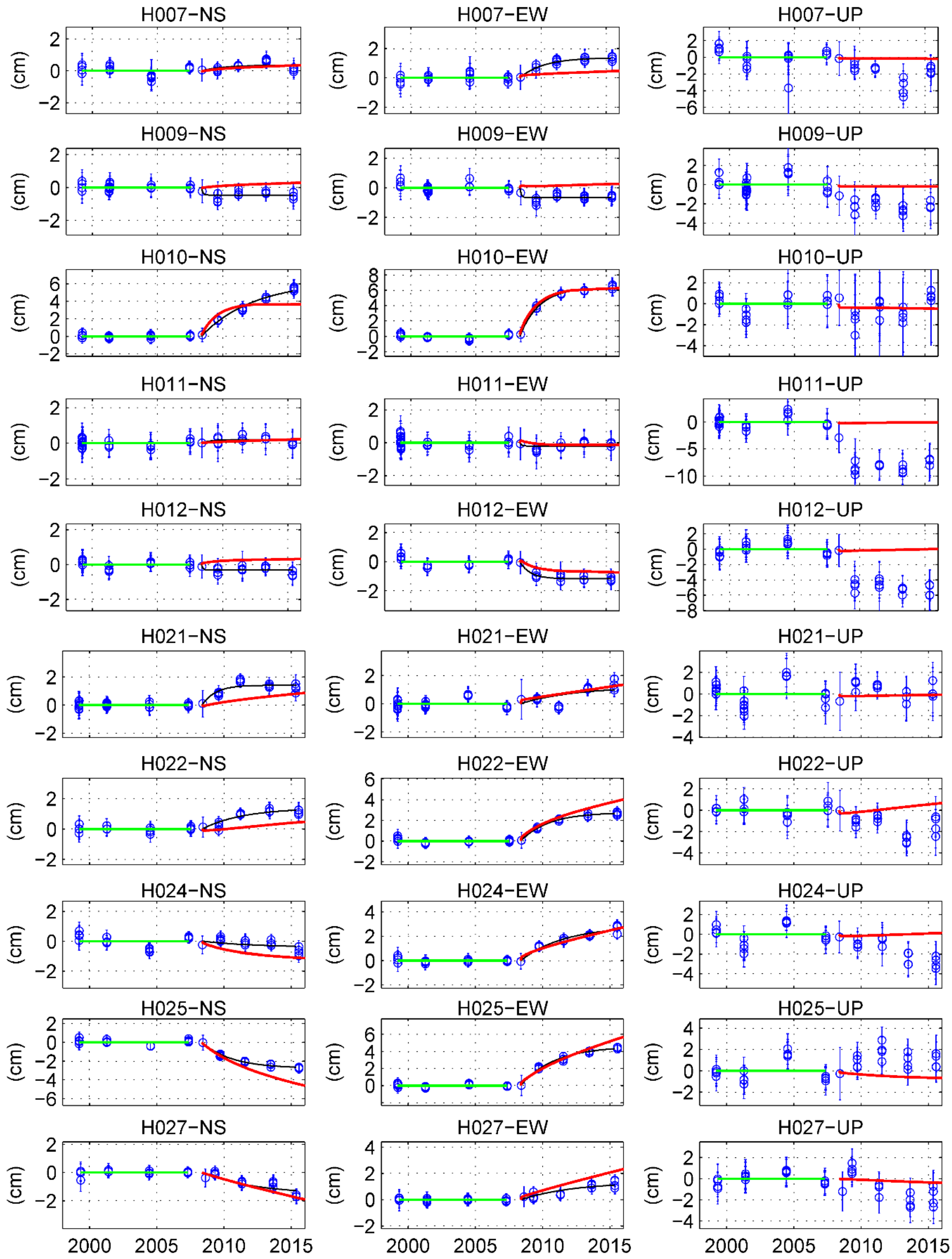

Figure S1. Displacement time series used in this study. The blue circles show the postseismic displacements with error bars of 95% confidence. Black and red curves represent the best-fit curve defined by Eq. (1) in the main text and the theoretical time series of the combined model. The green lines are the reference level obtained by removing the preseismic background trend.

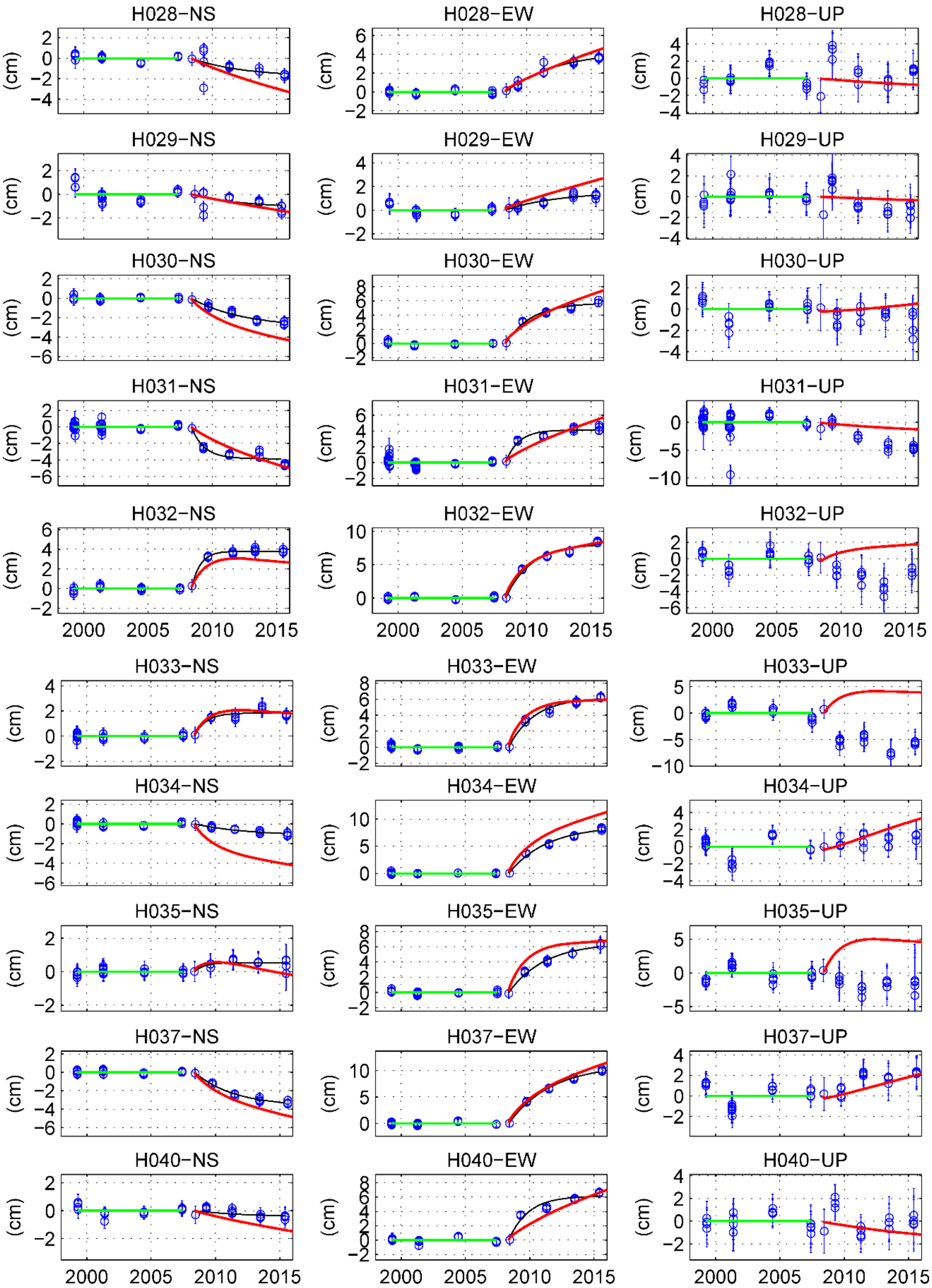

Figure S1 (continued)

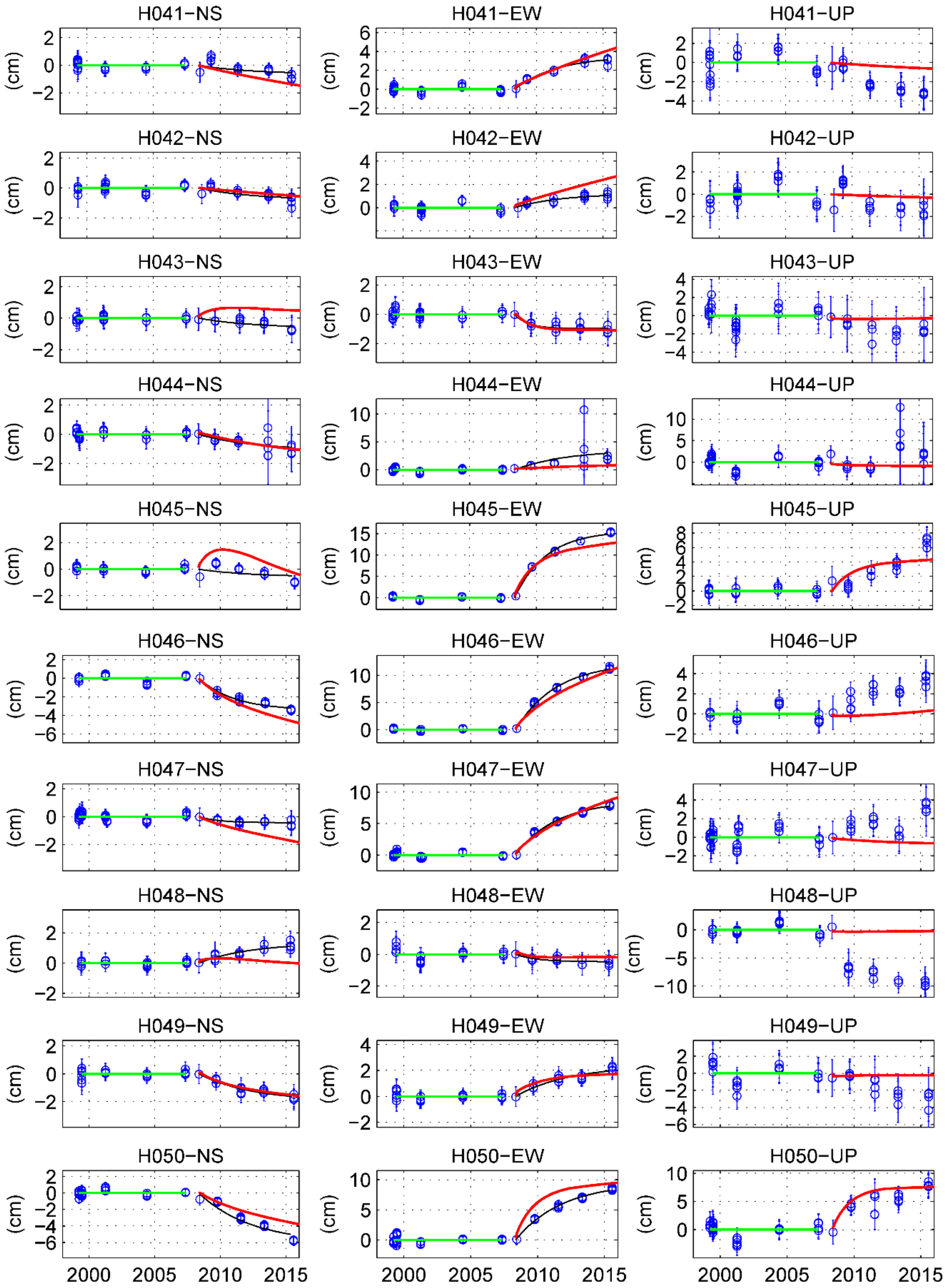

Figure S1 (continued)

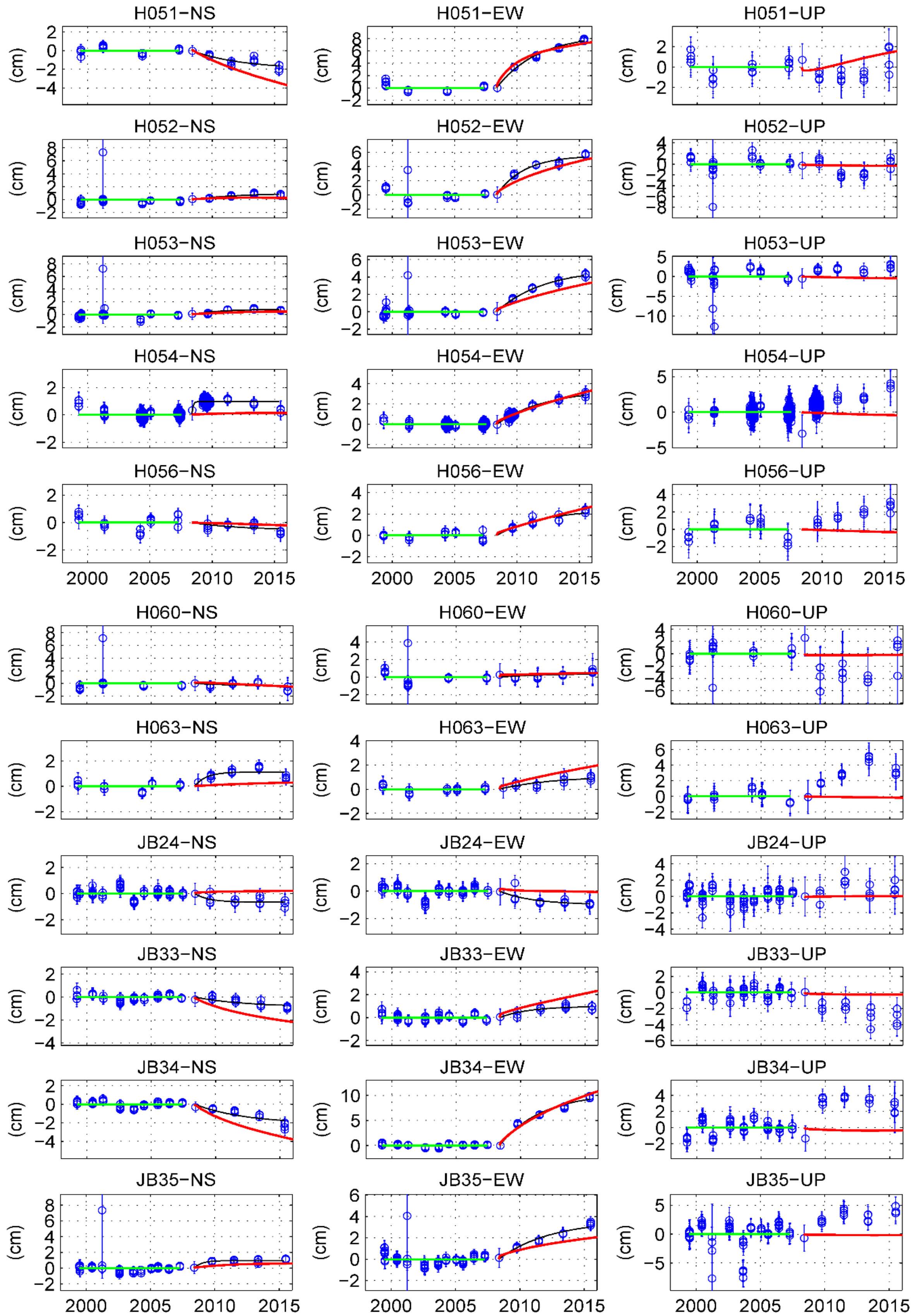

Figure S1 (continued)

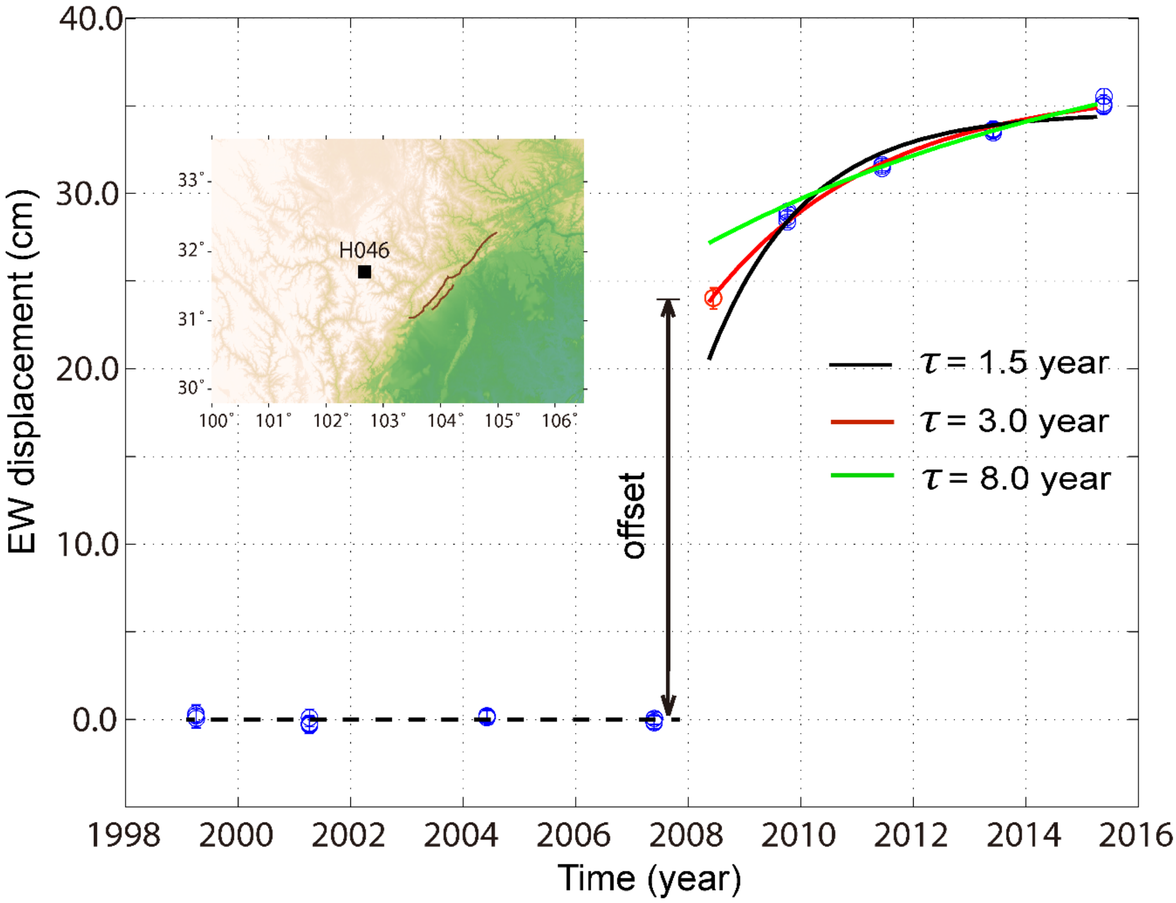

Figure S2. Example showing the curve fitting of the postseismic displacement time series. Curves with different colors represent the fitting with variable rise times. Blue circles are the data provided by Crustal Movement Observation Network of China (CMONOC), and the red circle is the quasi coseismic offset adopted from Wang et al. (2011).

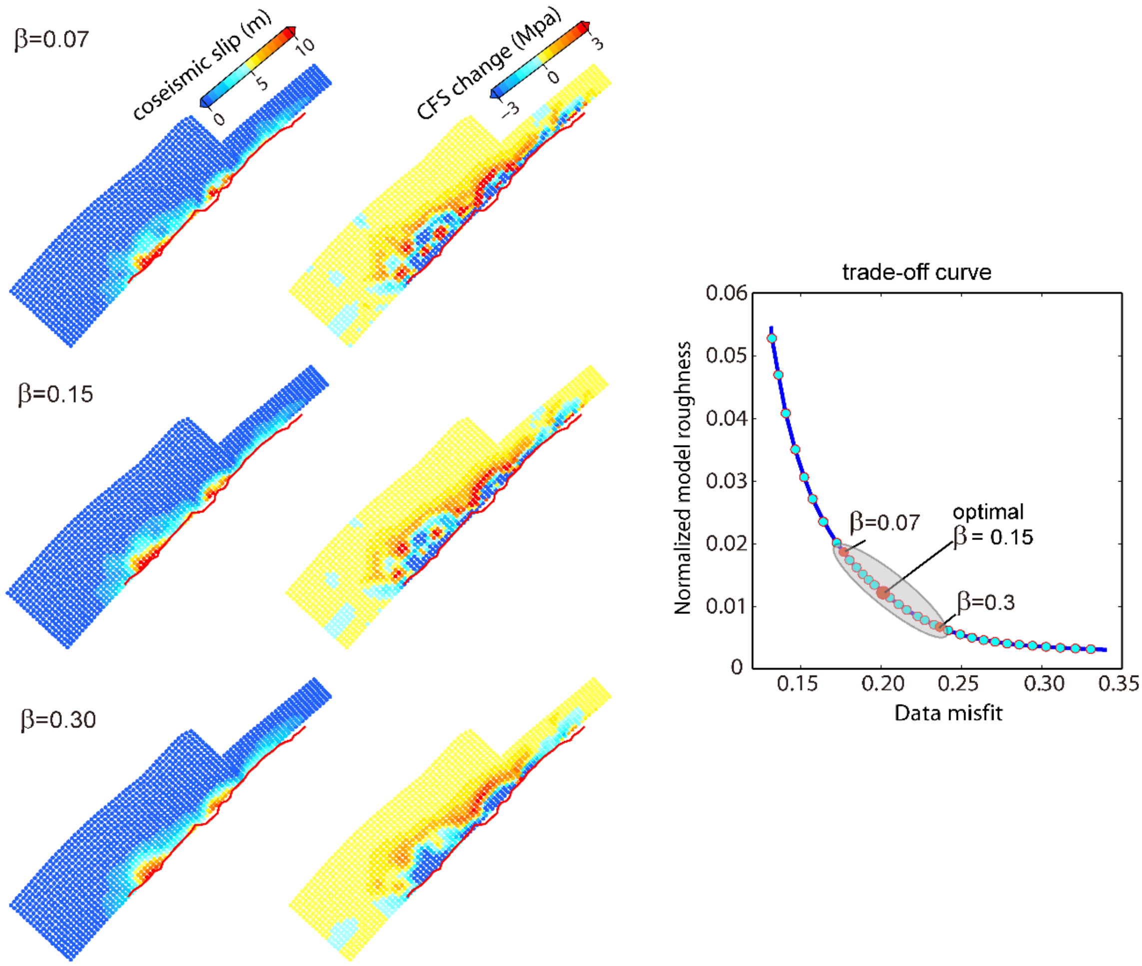

Figure S3. Results of coseismic slip inversion. Left: coseismic slip model and CFS change with variable smoothing factors; Right: trade-off curve with data misfit plotted as function of normalized model roughness. The shaded area shows the smoothing factors near the corner of the trade-off curve.

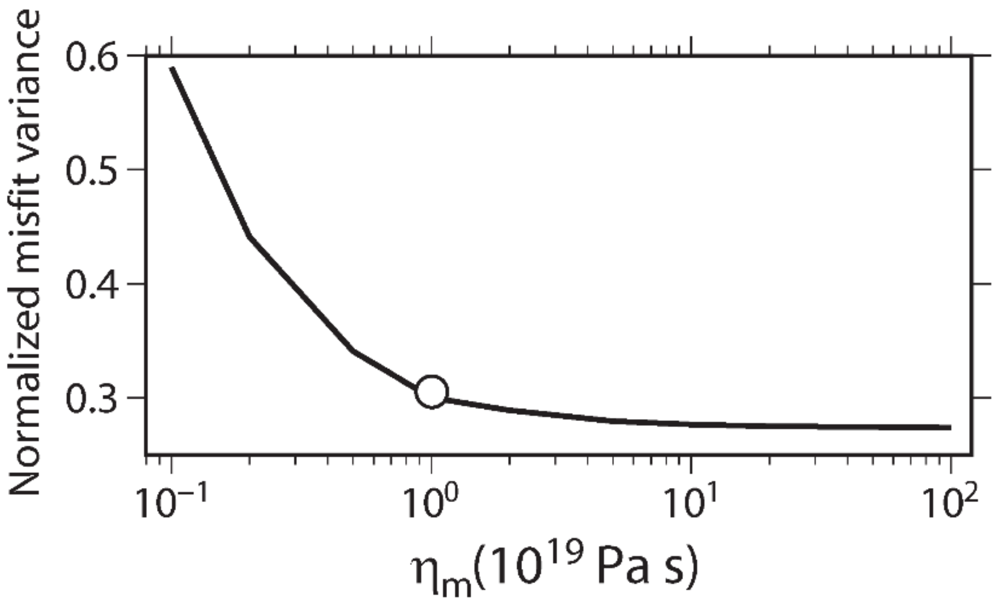

Figure S4. Normalized misfit variance of the pure viscoelastic relaxation model depending on the viscosity of the upper mantle beneath the Tibet Plateau (η_m), where the other viscosities are fixed at their optimal values (e.g., $\eta_T = 1.0 \times 10^{18}$ and $\eta_S = 1.0 \times 10^{20}$).

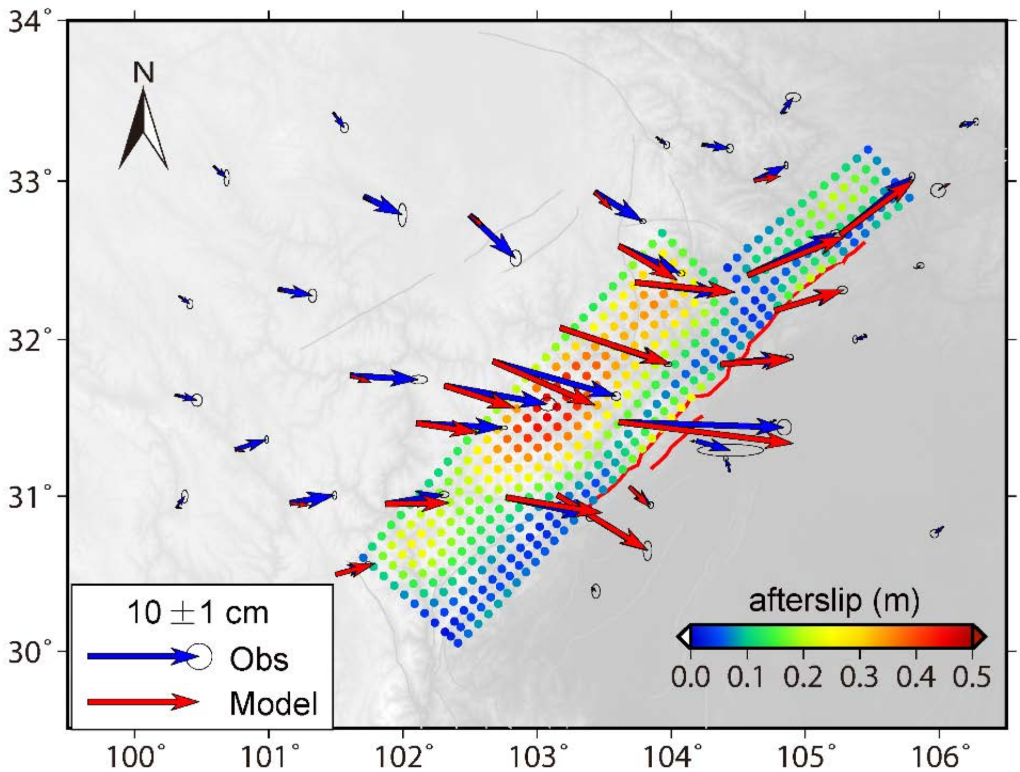

Figure S5. Afterslip distribution and data fitting for Model PAS-1 with the deep horizontal décollement limited at a length of 90 km.

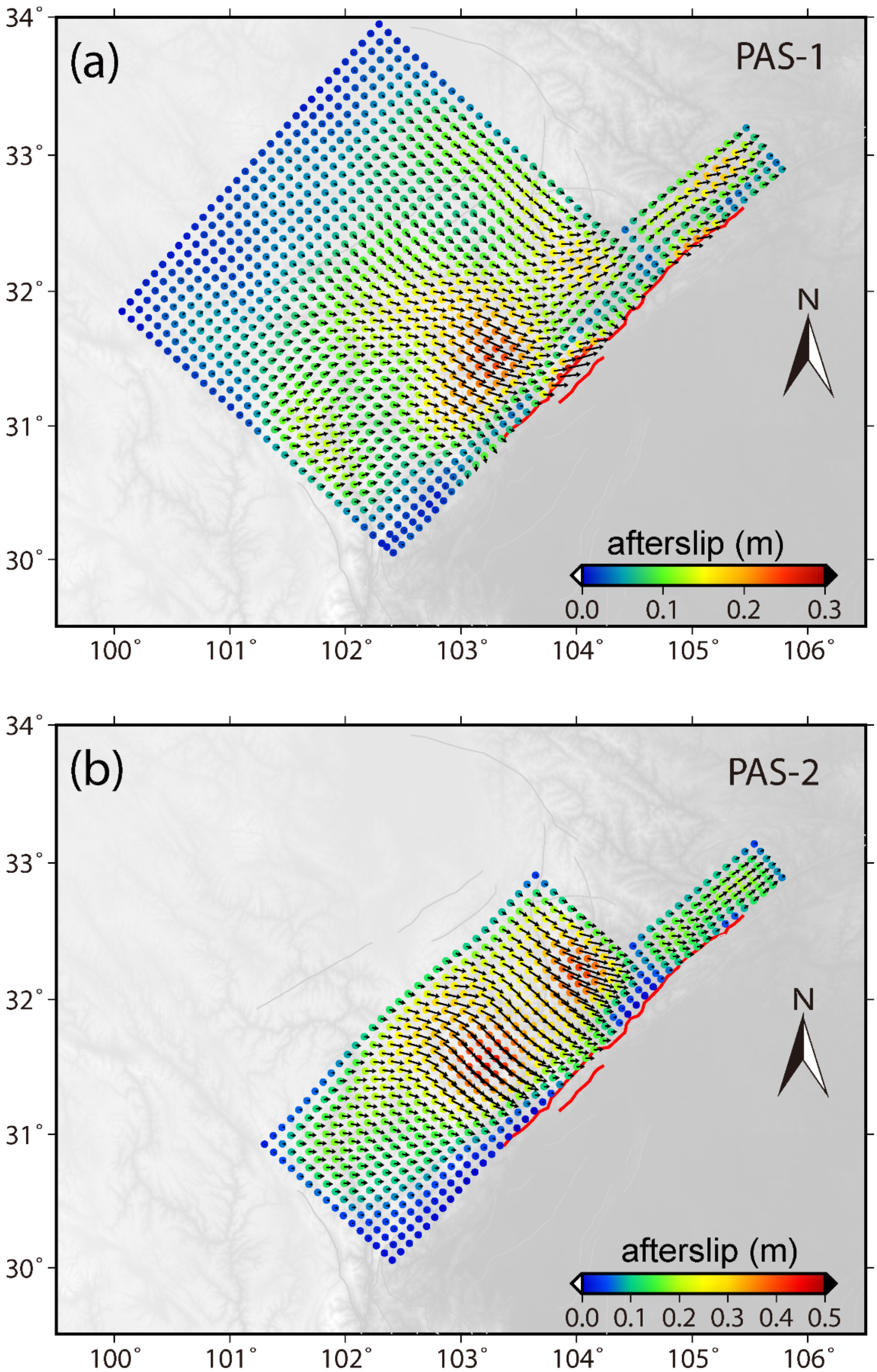

Figure S6. Slip distribution of the pure afterslip model with arrows showing the direction of slip on each fault patch.

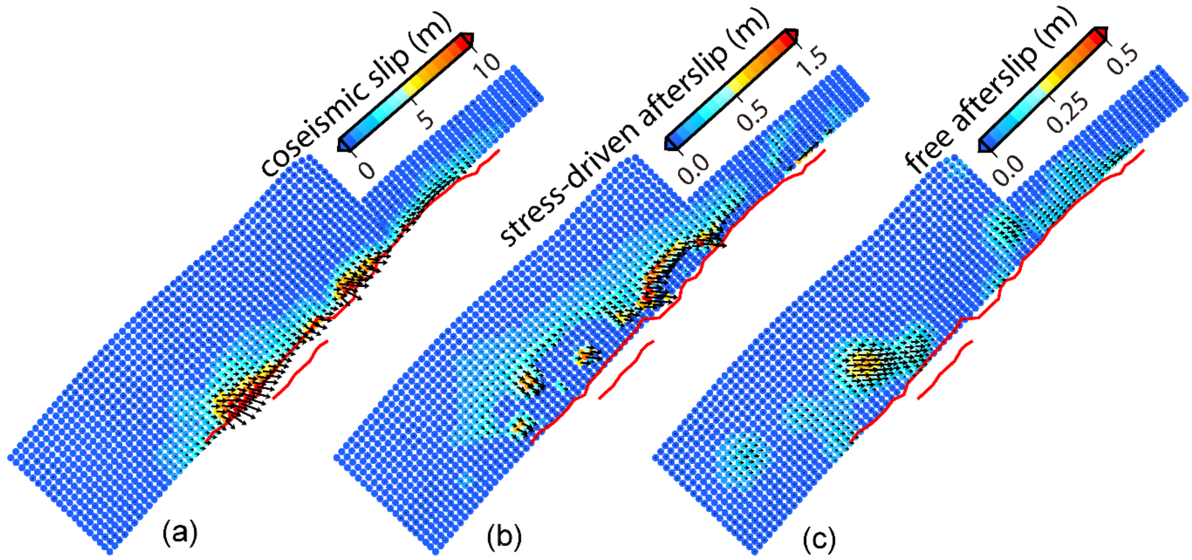

Figure S7. Slip distribution of the coseismic slip model, stress-driven afterslip model and free afterslip distribution derived from the residual data of the PVR model with arrows showing the direction of slip on each fault patch.

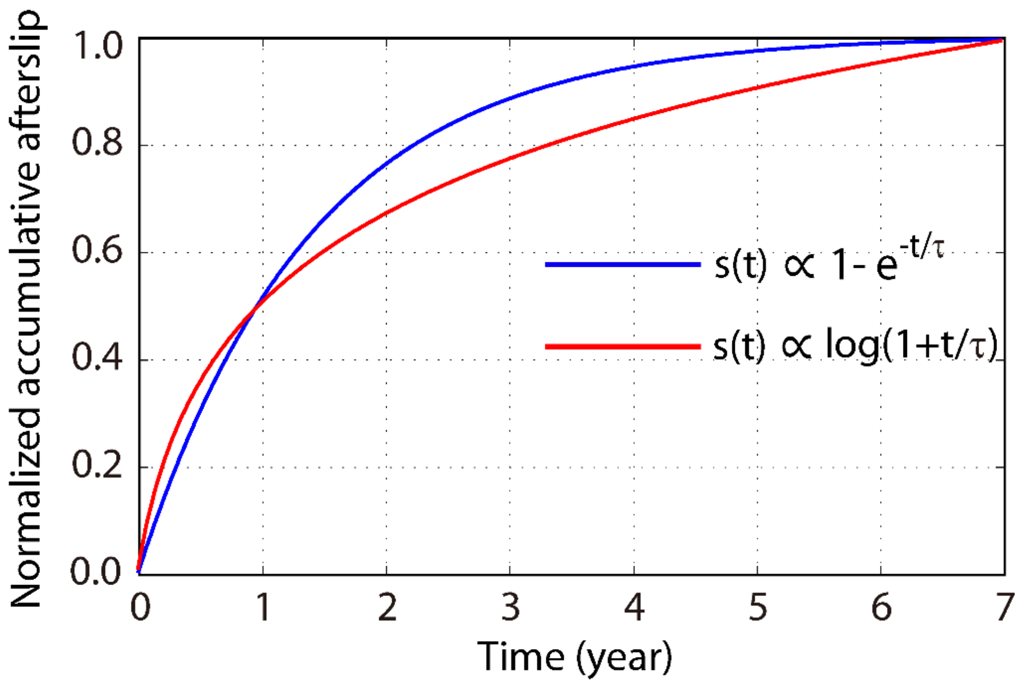

Figure S8. Comparison between two models for the time history of afterslip rate. The characteristic decay time τ used is 1.2 and 0.18 year for the blue and red curves, respectively.

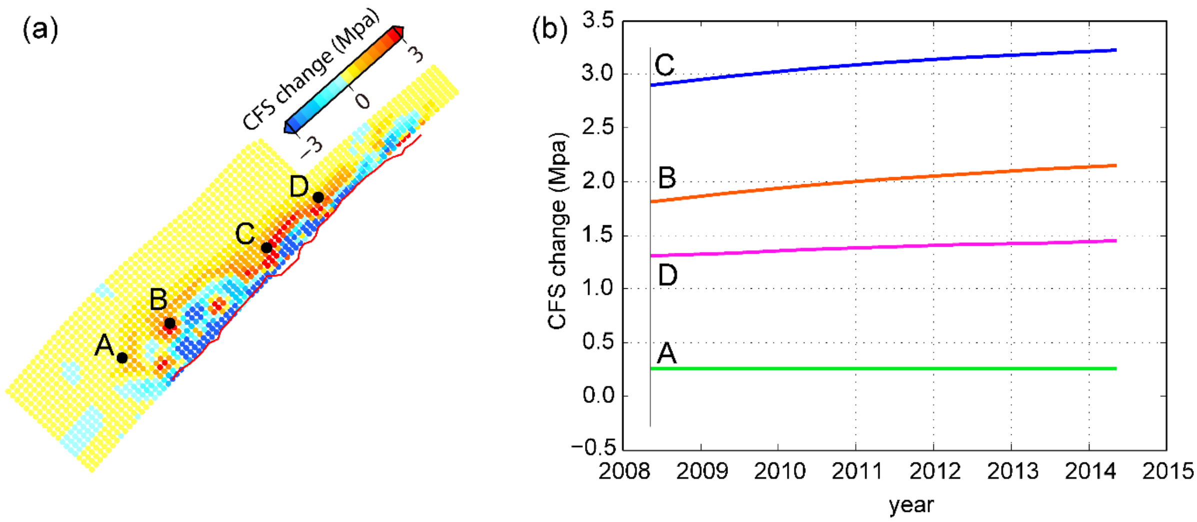

Figure S9. (a) CFS change on fault plane induced by coseismic rupture. (b) Temporal evolution of CFS changes caused by coseismic slip and viscoelastic relaxation on four typical points shown in (a). The gray line shows the time of the event. The start point of each line shows the coseismic CFS change.

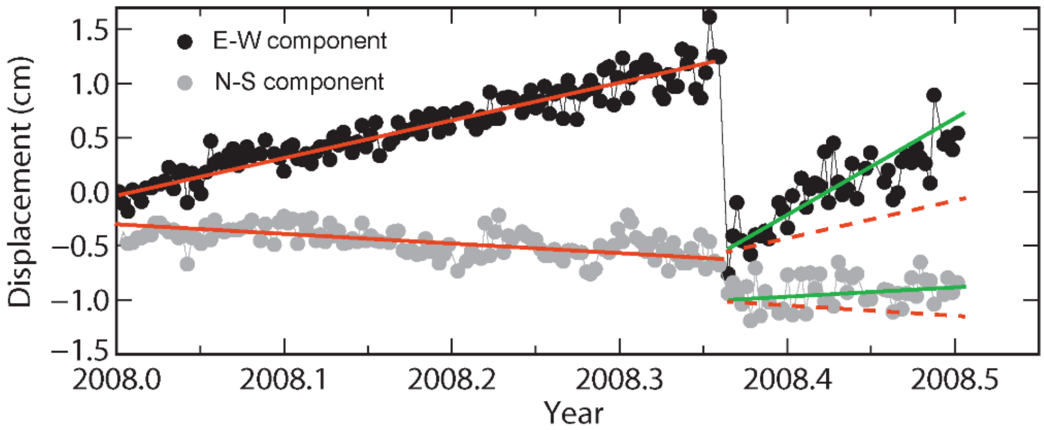

Figure S10. GPS displacement time series of Station QLAI before and after the Wenchuan earthquake (Wu et al., 2013). The two solid (or dashed in parallel) red lines show the pre-event linear trends for the two horizontal components, respectively, in comparison with the green lines for the post-event linear trends. The location of QLAI is shown in Fig. 1b in the main text.

Table S1. Postseismic displacements accumulated in the first 7 years after the Wenchuan earthquake.

Station	Longitude (deg)	Latitude (deg)	De (cm)	Dn (cm)	σDe (cm)	σDn (cm)
H007	106.155	33.340	1.34	0.35	0.09	0.13
H009	106.023	32.962	-0.66	-0.46	0.22	0.23
H010	105.226	32.571	6.31	5.16	0.11	0.15
H011	105.830	32.448	-0.20	0.20	0.17	0.11
H012	105.457	32.018	-1.18	-0.31	0.09	0.14
H021	104.824	33.423	0.99	1.41	0.30	0.17
H022	104.625	33.001	2.68	1.24	0.06	0.13
H024	104.226	33.228	2.50	-0.34	0.13	0.18
H025	103.435	32.931	4.32	-2.65	0.12	0.08
H027	101.482	33.429	1.11	-1.28	0.15	0.20
H028	101.706	32.902	3.56	-1.50	0.16	0.44
H029	100.595	33.093	1.25	-0.94	0.11	0.31
H030	103.613	32.591	5.57	-2.47	0.15	0.12
H031	102.500	32.786	4.12	-3.85	0.23	0.31
H032	104.571	32.405	7.90	3.81	0.27	0.09
H033	104.831	32.182	6.01	1.84	0.19	0.16
H034	103.732	32.361	7.89	-0.98	0.22	0.07
H035	104.444	31.802	5.98	0.55	0.18	0.12
H037	103.166	32.075	9.71	-3.31	0.15	0.10
H040	101.614	31.770	6.07	-0.37	0.35	0.15
H041	101.071	32.319	3.13	-0.54	0.17	0.26
H042	100.334	32.275	1.05	-0.65	0.12	0.19
H043	104.782	31.486	-0.97	-0.51	0.12	0.11
H044	104.187	31.353	2.94	-0.90	1.28	0.23
H045	103.612	31.474	14.87	-0.49	0.31	0.31
H046	102.670	31.850	11.04	-3.21	0.18	0.15
H047	102.096	31.466	7.77	-0.44	0.17	0.08
H048	104.441	31.157	-0.46	1.11	0.09	0.12
H049	103.692	31.060	1.96	-1.62	0.13	0.11
H050	103.145	31.008	8.21	-5.00	0.17	0.39
H051	102.775	30.992	7.59	-1.63	0.17	0.22
H052	101.866	30.949	5.31	0.82	0.21	0.10
H053	101.163	30.955	4.16	0.78	0.09	0.12
H054	100.750	31.297	2.84	0.97	0.06	0.13
H056	100.297	31.646	2.08	-0.46	0.21	0.20
H060	103.410	30.415	0.35	-0.37	0.16	0.25
H063	100.307	30.925	0.87	1.13	0.13	0.24
JB24	106.034	30.804	-0.92	-0.66	0.16	0.15
JB33	103.889	33.276	0.94	-0.71	0.11	0.15

JB34	102.306	31.706	9.22	-1.76	0.32	0.26
JB35	101.497	30.495	2.99	0.95	0.14	0.11

Reference:

Wu, Y. Q., Z. S. Jiang, M. Wang, S. Che, H. Liao, Q. Li, P. Li, Y. Yang, H. Xiang, Z. Shao, W. Wang, W. Wei, and X. Liu (2013), Preliminary results pertaining to coseismic displacement and preseismic strain accumulation of the Lushan M(S) 7.0 earthquake, as reflected by GPS surveying, Chin. Sci. Bull., 58, 3460-3466, doi: 10.1007/s11434-013-5998-5.

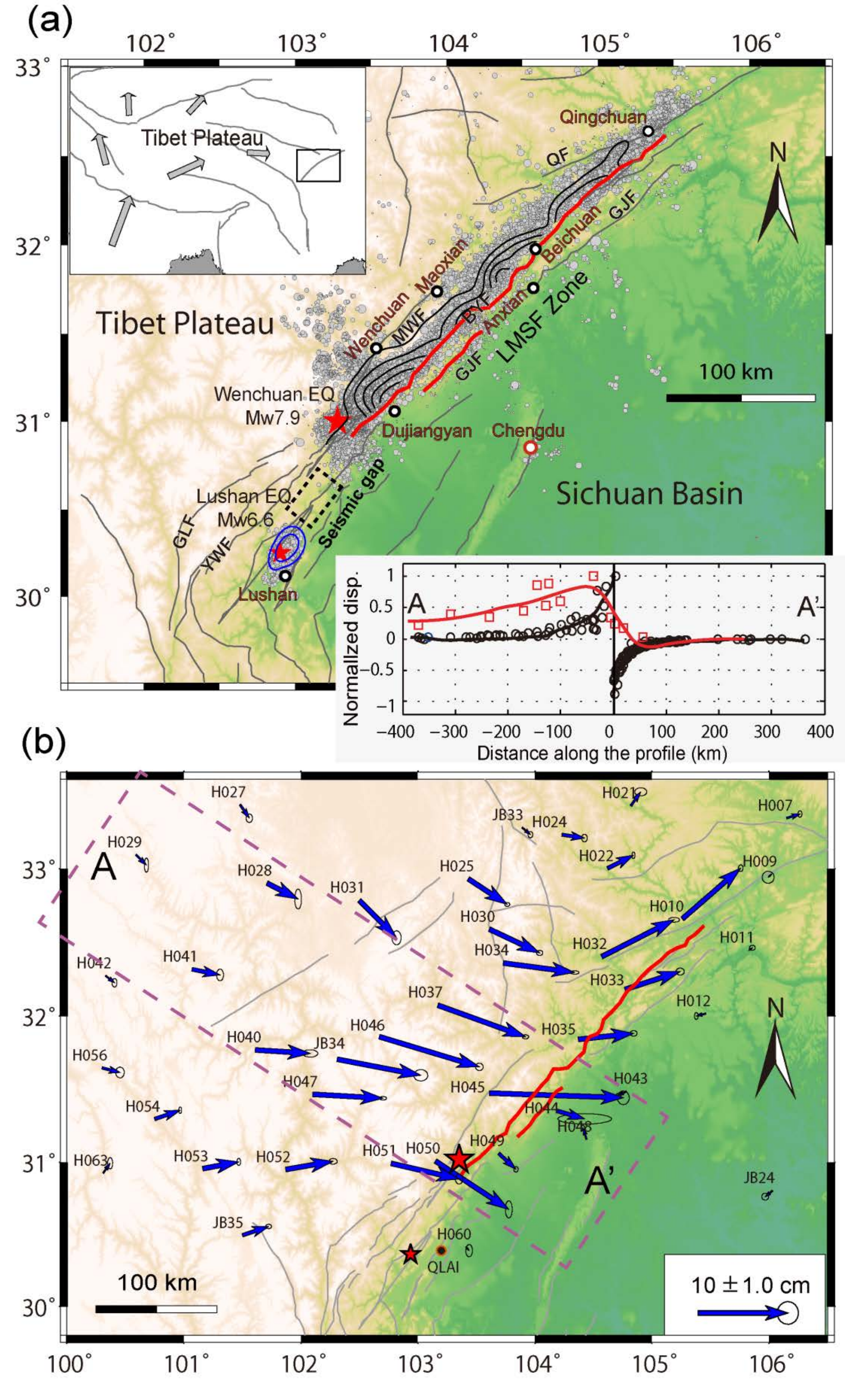

Figure 1. (a) Tectonic setting of the study area. The black and blue contours show the coseismic slip distributions of the 2008 Wenchuan (this study) and 2013 Lushan earthquakes (Jiang et al., 2014) projected on the surface using intervals of 2 m and 0.2 m, respectively. The thick red lines indicate the surface rupture trace

of the Wenchuan earthquake (Xu et al., 2009). The gray dots denote aftershocks of the two earthquakes that occurred within the first year (Fang et al., 2015). The dashed black box represents the seismic gap between the ruptures of the two earthquakes. (b) Observed cumulative postseismic surface displacements during the first 7 years after the Wenchuan earthquake. The gray lines represent the active faults in the study area. The blue vectors denote the observed postseismic displacements, and the ellipses mark the uncertainties with 95% confidence. The inset shows the normalized coseismic (black) and postseismic (red) displacement profiles from the area marked by the dashed violet rectangle. Abbreviations: GJF = Guanxian-Jiangyou Fault, GLF = Gengda-Longdong Fault, MWF = Maoxian-Wenchuan Fault, LMSF: Longmenshan Fault, BYF = Beichuan-Yingxiu Fault, QF = Qingchuan Fault.

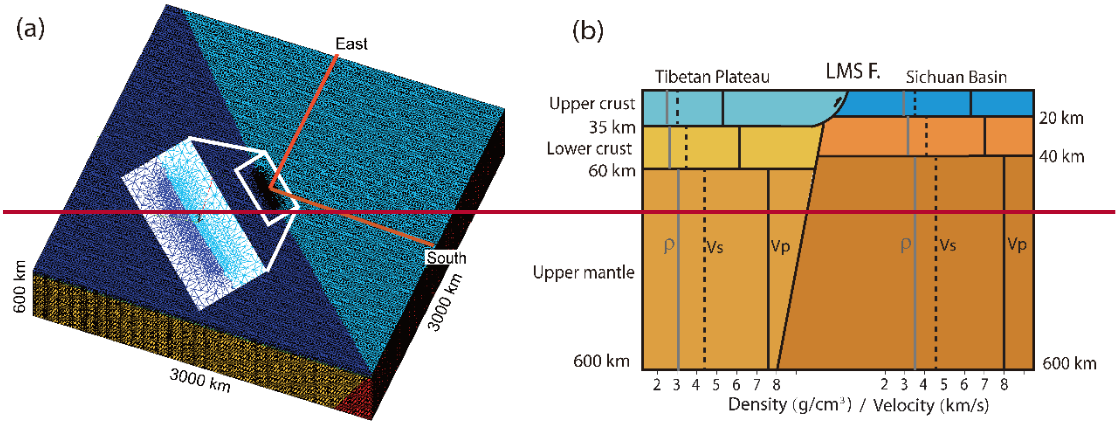

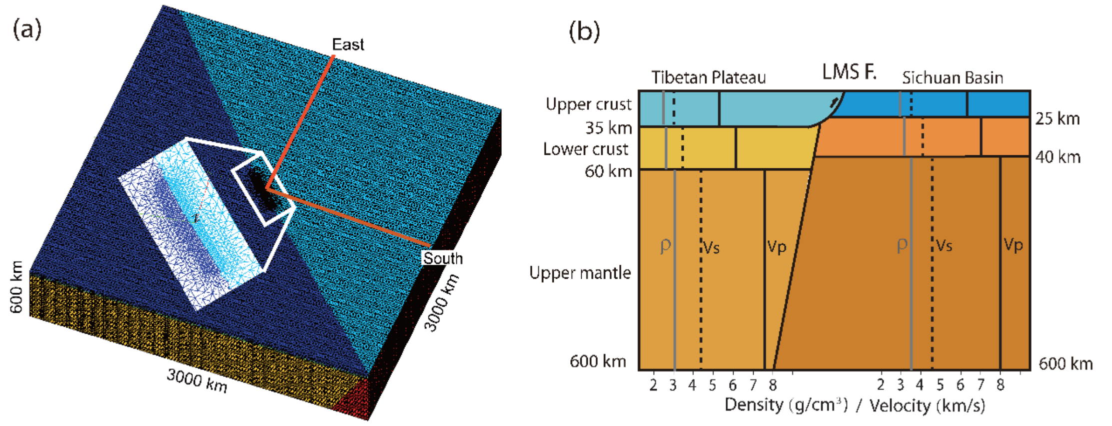

Figure 2. (a) Structure and mesh configuration of the finite element model. The element size increases from about 1 km for the near-fault region to about 50 km for the far-field region. (b) Sketch map and the 2D average structure across the Longmenshan fault.

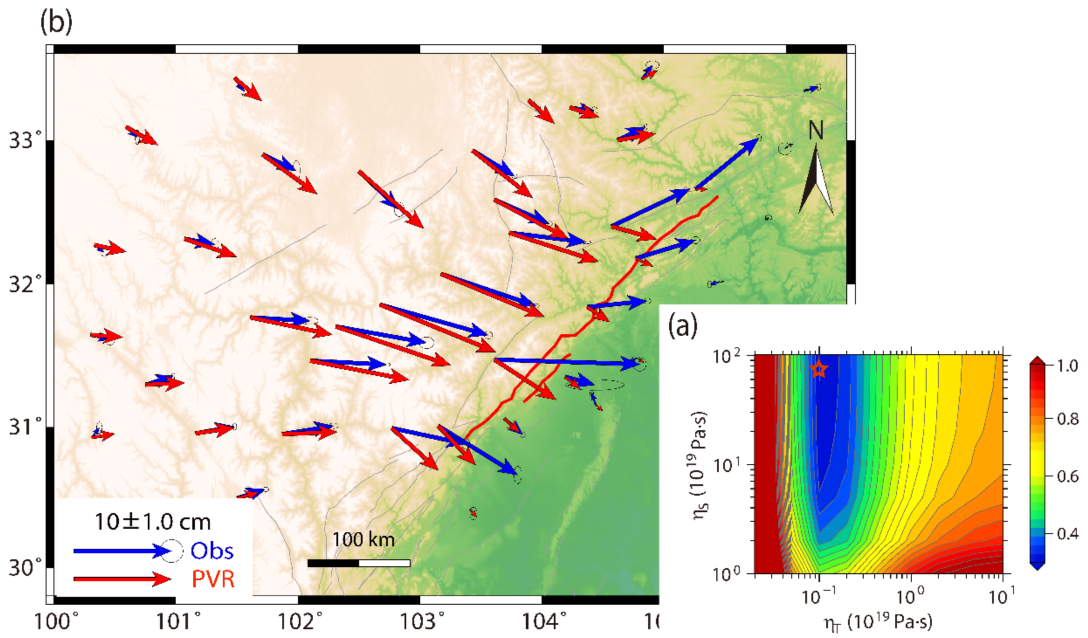

Figure 3. Results of the pure viscoelastic relaxation model (PVR). (a) Misfit variance (normalized by the data variance) as a function of the lower crustal viscosities of the Tibet Plateau (η_T) and the Sichuan Basin (η_S) used in the PVR model. (b) between the observed and predicted postseismic displacements in the first 7 years the Wenchuan earthquake.

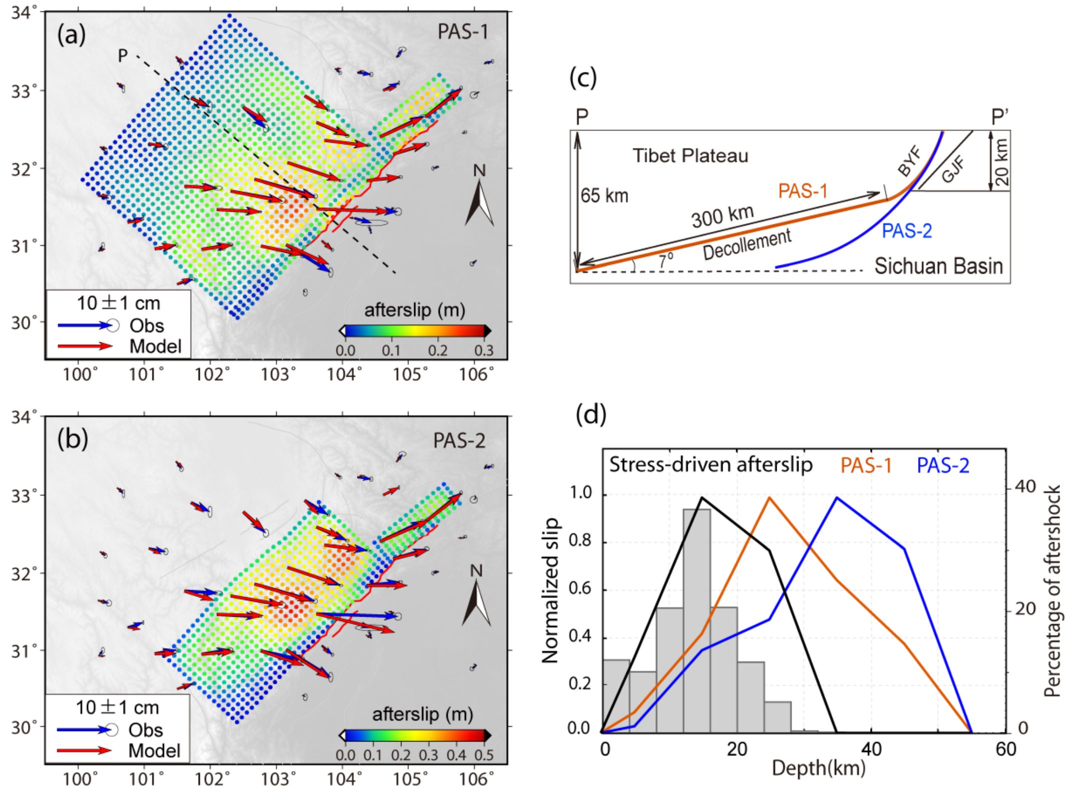

Figure 4. Comparison of the two pure afterslip models (PAS-1 and PAS-2). (a) and (b) Afterslip distributions and data fittings of Model PAS-1 and Model PAS-2, respectively. (c) Fault geometry of the two afterslip models on the profile P-P' marked in (a), where BYF and GJF represent the Beichuan-Yingxiu Fault and the Guanxian-Jiangyou Fault, as shown in Fig. 1. (d) Comparison of the aftershock seismicity (gray histograms with the right axis) and the two afterslip distributions with depth.

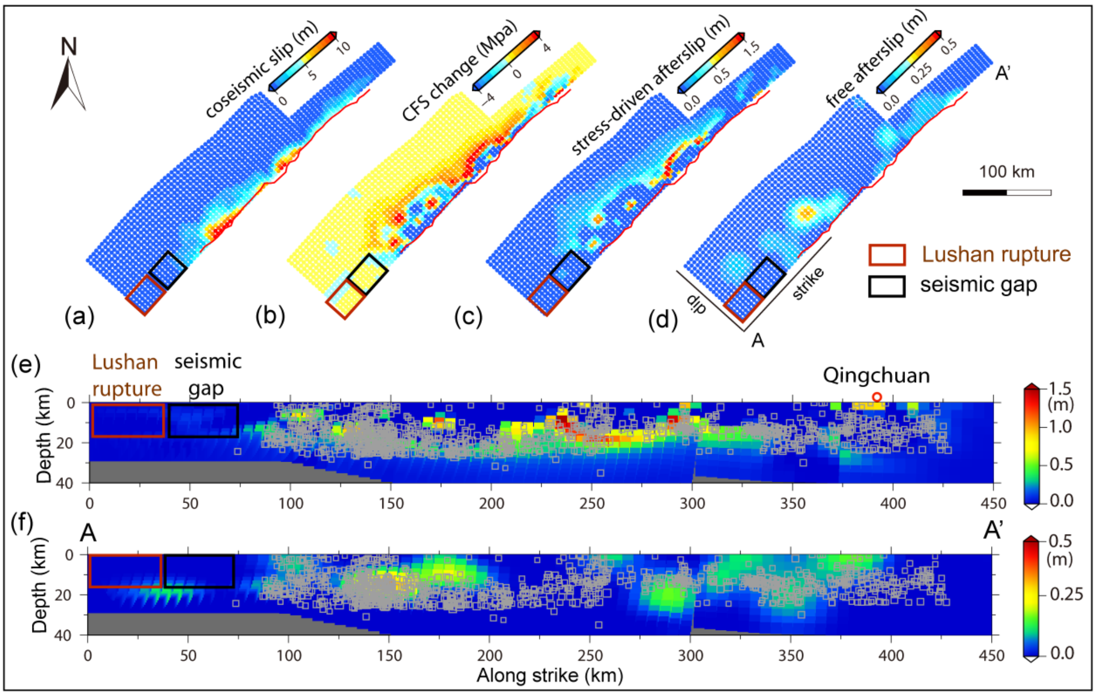

Figure 5. (a) Surface projection of the coseismic slip distribution. (b) Coseismic CFS changes on the fault plane. (c) Stress-driven afterslip distribution in the combined model. (d) Free afterslip distribution derived from the residual data of the PVR model. (e) and (f) Comparison of the aftershock (gray square) with the spatial distributions of the stress-driven afterslip and the free afterslip, respectively.

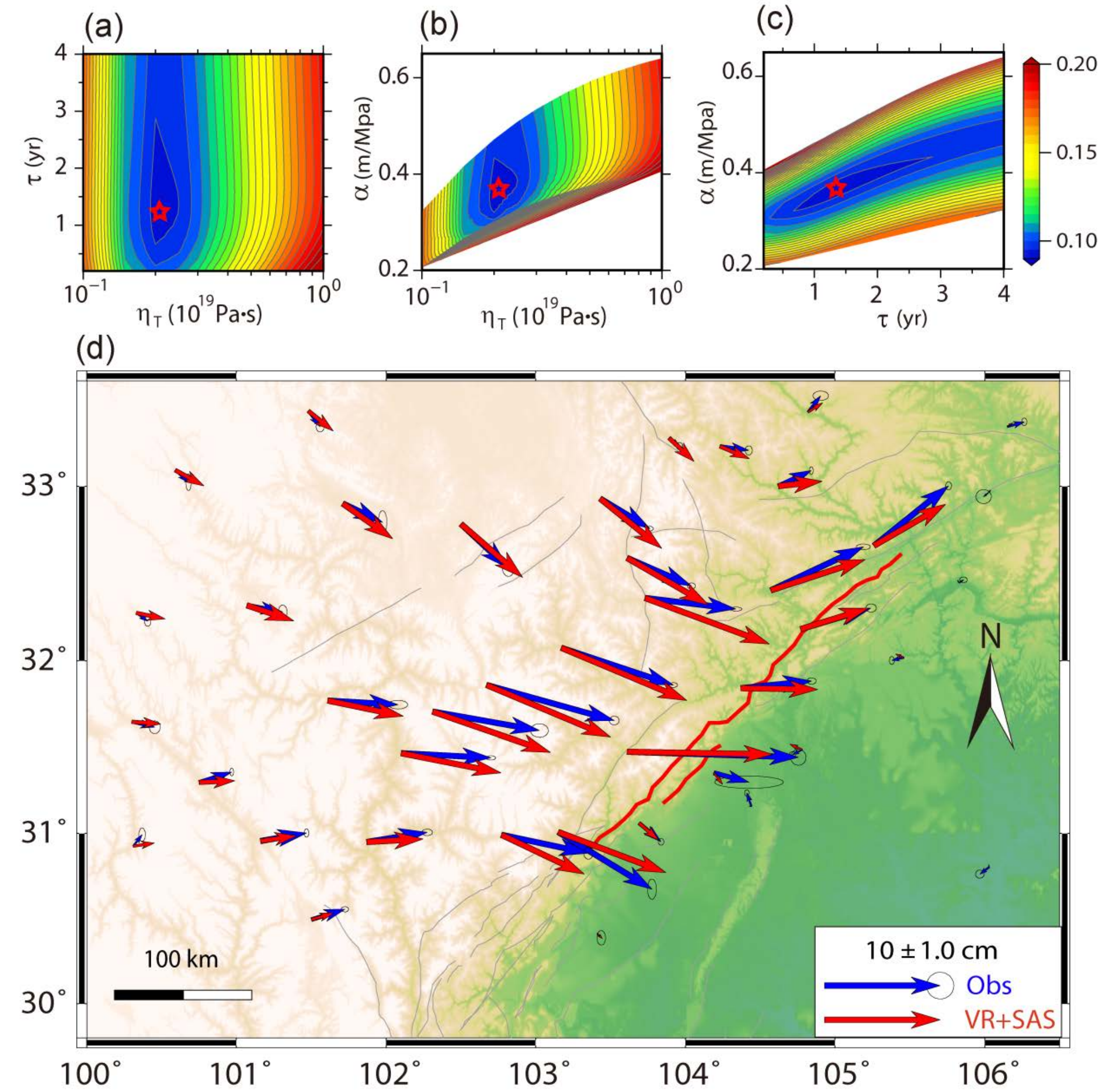

Figure 6. Results of the combined model (VR+SAS). (a)-(c) 3D map of the misfit variance (normalized by the data variance) projected on the (η_T, τ), (η_T, α) and (τ, α) planes, respectively, where η_T is the lower crustal viscosity of the Tibet Plateau, τ is the characteristic decay time of the afterslip, and α is the scaling factor between the afterslip and the coseismically induced positive Coulomb stress change. The red star marks the minimum of the misfit variance, which defines the location of the 3 optimal model parameters. (d) Comparison between the observed and predicted postseismic displacements in the first 7 years after the Wenchuan earthquake.

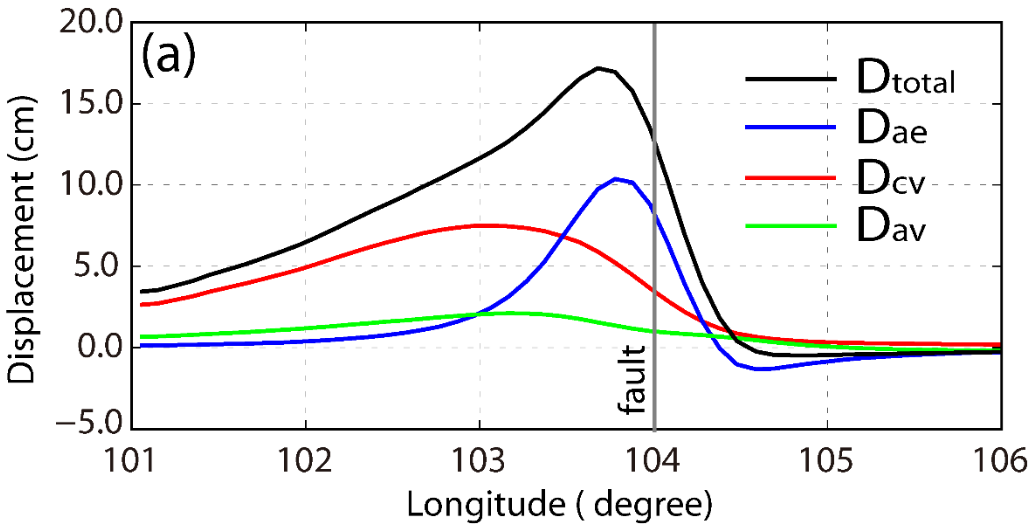

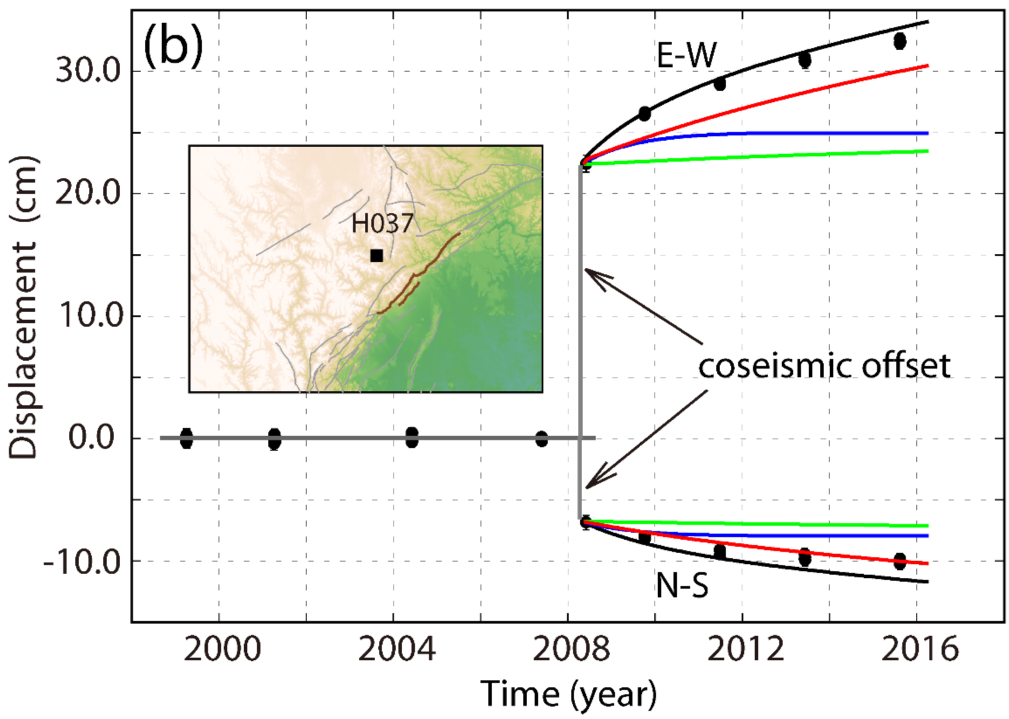

Figure 7. Contributions of different deformation processes to the observed postseismic surface displacement. (a) East component of the 7-year postseismic displacement along the profile P-P' shown in Fig. 3a, predicted by the combined model. D_{cv} is the postseismic viscoelastic effect induced by the coseismic slip, D_{ae} and D_{av} are the elastic and viscoelastic effects induced by the aseismic afterslip, respectively. (b) The different effects in the time domain on a selected station (H037). The colour coding is the same as used in (a).

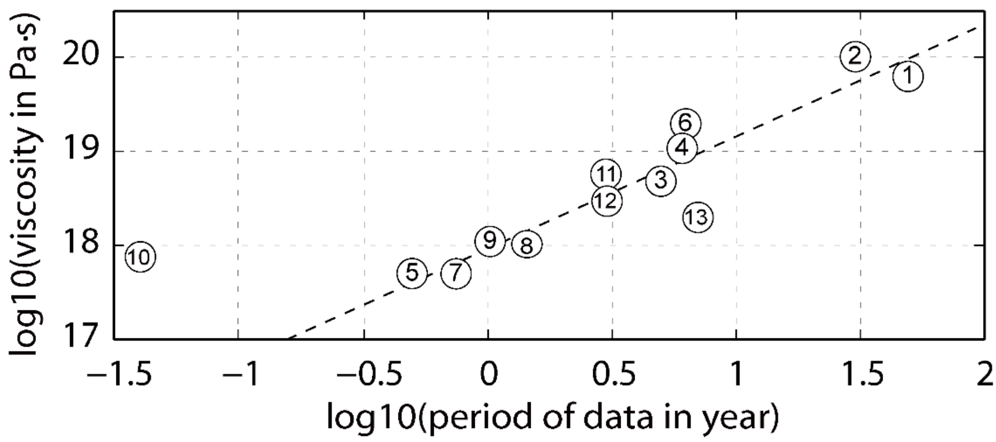

Figure 8. Effective lower crustal viscosities beneath the Tibet Plateau inferred by using postseismic geodetic data covering different time periods and for different earthquakes published in recent years (Table 1).